FABRICATION AND CHARACTERIZATION OF ELECTRONIC AND OPTOELECTRONIC DEVICES USING SEMICONDUCTOR NANOMEMBRANES

By

Munho Kim

A dissertation submitted in partial fulfillment of the requirements for the degree of

Doctor of Philosophy

(Electrical and Computer Engineering)

At the

UNIVERSITY OF WISCONSIN-MADISON

2016

Date of final oral examination: 05/06/2016

The dissertation is approved by the following members of the Final Oral Committee:

Zhenqiang Ma, Professor, Electrical and Computer Engineering

Luke Mawst, Professor, Electrical and Computer Engineering

Zongfu Yu, Assistant Professor, Electrical and Computer Engineering

Shaoqin Gong, Professor, Biomedical Engineering

Xudong Wang, Associate Professor, Materials Science and Engineering

To my family

Acknowledgement

I am very thankful for the following funding agencies/programs: AFOSR, ONR, NSF, ARO, DARPA, and WARF for their financial sponsorship on the projects that I have been involved in.

My research has never been possible without the guidance of my committee professors and support from my colleagues and friends. Firstly, I would like to express my deepest gratitude to my advisor Prof. Zhenqiang (Jack) Ma for his constant guidance, enlightening, and scholarship support through my Ph. D. study. I would also like to thank Prof. Luke Mawst, Prof. Shaoqin (Sarah) Gong, Prof. Xudong Wang, and Prof. Zongfu Yu for their valuable comments and suggestions on my research and thesis.

I would like to thank Wisconsin Center for Microelectronics (WCAM) staffs, Dan Christensen, Hal Gilles, Kurt Kupcho, Quinn Leonard, and Felix Lu.

I would like to thank our former group members, Dr. Han Zhou, Dr. Kan Zhang, Dr. Gui Gui, Dr. Wenjuan Fan, Dr. Kanglin Xiong, Dr. Hongyi Mi, Dr. Minkyu Cho, Dr. Solomon Mikael, and Dr. Cuong Manh Nguyen.

I would like to thank our group members, Dr. Jung-Hun Seo, Dr. Dong Liu, Dr. Tzu-Hsuan Chang, Namki Cho, Dong-wook Park, Jaeseong Lee, Sang June Cho, Yei Hwan Jung, Firat Yasar, Tong June Kim, Kwangeun Kim, Huilong Zhang, Zhenyang Xia, Juhwan Lee, Hyungsoo Kim, Jae Ha Ryu, Jeongpil Park, Jisoo Kim, and Jihye Bong.

I could not express how thankful I am for the support from my family and parents. My Ph. D. study would not have been possible without my wife, Youngmi Mun and my two little babies, Hannah Kim and Hale Kim.

Abstract

Semiconductor nanomembrane (NM) is a thin-film semiconductor layer which can be released from its donor wafer. Typical thickness ranges from several tens of nanometer to hundreds nanometer. In recent years, the semiconductor NMs have been drawing more interest due to their unique material properties and versatile applications. One of the most popular NM is a Si NM released from Si-On-Insulator (SOI) using a hydrofluoric acid (HF) undercut process. Because a buried oxide layer (BOX, SiO_2) has a large etching selectivity against the Si in HF, the Si NM can be easily detached from the SOI and transferred to any types of substrates using a Polydimethylsiloxane (PDMS) stamp. Several advantages that make it suitable for high performance electronic and optoelectronic devices are single crystallinity, high flexibility, reliable transfer methods, and compatibility with Si based fabrication techniques. Other types of NMs are Ge NM, GaAs NM, and GaN NM.

In this thesis, novel electronic and optoelectronic applications, including tunable biaxial compressive strained Si NM, resonant tunneling diodes, Ge on insulator (GeOI), and flexible Ge NM metal-semiconductor-metal (MSM) photodiodes, are designed and implemented.

A method of creating tunable and programmable biaxial compressive strain in Si NMs transferred onto a Kapton® HN polyimide film has been demonstrated. The programmable biaxial compressive strain (up to 0.54%) was generated utilizing a unique thermal property exhibited by the Kapton HN film, namely, it shrinks from its original size when exposed to elevated temperatures. The correlation between the strain and the annealing temperature was carefully investigated using Raman spectroscopy and high resolution X-ray diffraction. It was found that various amounts of compressive strains can be obtained by controlling the thermal annealing temperatures. In addition, a numerical model was used to evaluate the strain distribution in the Si

NM. This technique provides a viable approach to forming in-plane compressive strain in NMs and offers a practical platform for further studies in strain engineering.

A novel method of creating multiple barrier heterostructures by using transferrable single crystalline Si NMs and aluminum oxide (Al_2O_3 layers deposited by an atomic layer deposition (ALD) system is presented. The crystalline structure of the Al_2O_3/Si NM quantum well was examined using transmission electron microscopy (TEM). In addition, X-ray photoelectron spectroscopy (XPS) confirmed the existence of potential wells between the Si NM and Al_2O_3. As an example demonstration, we fabricated double barrier (DB) and triple barrier (TB) Al_2O_3/Si NM resonant tunneling diodes (RTDs) and the devices exhibited a high negative differential resistance (NDR) at room temperature (RT) which was only predicted theoretically. The successful demonstration of the single crystalline semiconductor-amorphous oxide quantum well and its example device open a new pathway to forming various types of quantum wells that cannot be formed by conventional epitaxial growth techniques. More importantly, it allows realization of quantum electronic devices operating at RT by a distinct quantum confinement.

Optical loss in silicon (Si) waveguide can be reduced if longer (e.g., >1.55 μm) wavelength is used. However, light absorption coefficients of Ge, which is the most important light detection material in Si photonics, degrade rapidly beyond 1.55 μm. Therefore, extending the use of Ge for Si photonics into longer wavelengths by enhancing the light absorption coefficient of Ge beyond 1.55 μm is of significant importance. In this study, the light absorption property of Ge NM, which incorporates hydrogen (H), in near-infrared (NIR) wavelength range was analyzed. The H was introduced into the Ge layer of GeOI wafer during GeOI fabrication. The H ions combined with ion implantation induced Ge vacancies form V_2H that acts as electrically active acceptor. The refractive index and the extinction coefficient of the Ge layer exhibit changes that were caused by

the H incorporation. Due to the presence of the large amount of acceptors, the light absorption coefficient of the Ge layer becomes much higher (10 times) than that of bulk Ge in the wavelength range of 1000 ~ 1600 nm. Increased light absorption was further measured from released Ge NM that has H incorporation in comparison to that of bulk Ge, proving the enhanced light absorption coefficient of H incorporated Ge. Thermal anneal of the GeOI diffused out some of the incorporated H and thus slightly reduced the light absorption coefficients (still higher than that of bulk Ge). Finally metal-semiconductor-metal (MSM) photodetectors were demonstrated using the H incorporated Ge on GeOI.

Flexible Ge NM based MSM photodiodes are demonstrated. The effect of uniaxial tensile strain in Ge NM based photodiode was investigated using bending fixture. Dark current density is decreased from 21.5 to 4.8 mA/cm^2 at 3 V by tensile strain of 0.42% while responsivity is increased from 0.2 to 0.45 A/W at 1.5 μm. Enhanced responsivity is also observed at longer wavelengths up to 1.64 μm. The uniaxial tensile strain effectively reduces the direct bandgap energy of the Ge NM, leading to shift of the absorption edge toward a longer wavelength.

TABLE OF CONTENTS

LIST OF FIGURES

Chapter 1. Transferrable semiconductor nanomembrane for electronic and optoelectronic devices

1.1 Introduction

In recent years, a number of various types of flexible electronic and optoelectronic devices have been reported. Typical example devices are flexible photodetectors (PDs) and thin-film transistors (TFTs).[1-5] They have merits such as light-weight, bendability, and high performance. In general, amorphous or organic semiconductors are the main platform used to fabricate the flexible devices.[6,7] However, low carrier mobility which originates from its material property is one disadvantage and makes it difficult to be used for high speed applications.[8] In addition, the organic semiconductors are not compatible with the advanced silicon (Si) based technology. To enhance the device performance, polycrystalline Si (pc-Si) with a larger grain size was employed in the fabrication of TFTs.[9] Mobility of the pc-Si increases with grain size because a small grain boundary reduces scattering and trapping sites. However, the speed of the pc-Si based TFTs is still low compared to that of the TFTs made from single crystalline Si.

Thin-film semiconductor is a building block for various electronic and optoelectronic devices. Especially, semiconductor nanomembranes (NMs), a more refined form of the thin-film semiconductor, have enabled novel research topics from both semiconductor device physics and material science.[10,11] Since the thickness of NM range from several hundreds to tens of nanometers, it is a good candidate as an active material for flexible purposes. Its thinness allows for bendability while maintaining its great material properties from its bulk counterpart. Transferrable semiconductor NMs are released from the donor substrate and become free-standing by transfer techniques. These free-standing NMs provide more versatilities such as flexibility and single

crystallinity. In addition, novel combination of material integration is possible to form heterogeneous junction via NM transfer. Advantages of the transferrable NMs and its device applications will be further discussed in the following sections.

1.2 Advantages of transferrable semiconductor NMs

The transferrable semiconductor NMs show several advantages which make it suitable for high performance flexible applications. It includes single crystallinity, high bendability, reliable transfer techniques, and compatibility with Si-based fabrication technology.

Si nanomembranes (Si NMs) and Ge nanomembranes (Ge NMs) are released from Si-on-insulator (SOI) and Ge-on-insulator (GeOI) wafers, respectively. A thin Si or Ge layer is delaminated from its bulk wafer via exfoliation process by hydrogen (H+) implantation and subsequent annealing.[12] The exfoliated film is bonded to a thermally oxidized Si wafer. Single crystallinity of Si NM and Ge NM is preserved since the implantation damaged layer is mostly removed by the chemical and mechanical polarization (CMP) process. This guarantees its similar carrier mobility and bandgap structure compared to bulk materials. High carrier mobility along with high bendability make it an attractive material platform for flexible devices. The carrier mobility of Si and Ge is much higher than that of its amorphous or polycrystalline counterparts. It also exceeds the carrier mobility of organic semiconductor materials. This superior property enables the devices to perform in the giga-hertz region with improved direct-current (DC) and radio-frequency (RF) characteristics.

The thickness of the NM can be conveniently tuned beforehand via thinning techniques. For Si NM, thermal oxidation (either dry or wet oxidation) and subsequent removal of the grown

oxide (silicon dioxide, SiO_2) using hydrofluoric acid (HF) reduces the thickness of the Si NM. This technique could achieve a thickness of less than 10 nm with good controllability. For Ge NM, reactive ion etching (RIE) with SF_6 or CF_4 gas can be used to thin down Ge since thermal oxidation of Ge is not applicable. Although thinning by RIE is less reliable than thermal oxidation in terms of thickness uniformity, it provides a decent approach to thinning Ge NM.

1.3 Transfer printing of semiconductor NMs

A reliable transfer technique is critically important to achieve NM-based flexible devices or heterogeneous junctions. Transfer printing is a unique technique that releases the NMs or finished devices from the donor substrate and moves them onto foreign substrates. The most well-known material for the transfer is SOI with a sacrificial layer (SiO_2). Because SiO_2 has a large etching selectivity against Si in HF, Si can be easily released from the SOI and transferred to any types of substrates using a Polydimethylsiloxane (PDMS) stamp. A detailed process about the undercut and transfer of the Si NM is shown in Figure 1.1.[13]

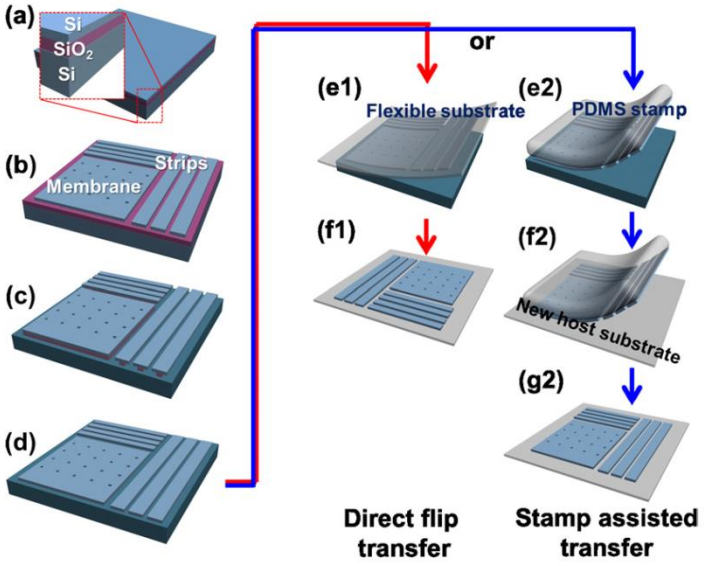

Figure 1.1 *Undercut and transfer process of the Si NM:* ***(a)*** *Vertical structure of the SOI wafer.* ***(b)*** *Photo lithographically patterning and dry etching to remove unwanted Si areas.* ***(c)*** *Immersing the sample in HF solution to release the Si NMs.* ***(d)*** *Released Si NMs gently fall and stick to bottom Si substrates via van der Waals forces.* ***(e1-f1)*** *Si NM transfer on a flexible substrate using a sticky layer (i.e., SU-8).* ***(e2-f2-g2)*** *NM pick up by a PDMS stamp and manual transfer of Si NM to a new host substrate.*

Direct flip transfer utilizes an adhesive layer (e.g., SU8-2002) coated on the target substrate. This method is usually applied to transfer the NMs onto the flexible substrates such as polyethylene terephthalate (PET) and Kapton films. The NMs will be transferred on the adhesive layer coated target substrate by pressing the NMs and peeling up against the substrate. Since the NMs are flip-transferred, it may need some design consideration such as doping profile. Stamp-assisted transfer utilizes an elastomeric PDMS stamp to pick up the NMs and transfer them onto the target substrate. No adhesive layer is required and this enables direct contact to other semiconductors. This opens a new possibility for novel heterogeneous integration which is not possible by conventional epitaxial growth techniques.

1.4 Novel electronic and optoelectronic devices

Researchers have successfully introduced many applications using semiconductor NMs.[14-16] Figure 1.2 shows examples of flexible electronic and optoelectronic thin-film devices. Two merits (i.e., flexibility and single crystallinity) are clearly demonstrated. The devices can be bent with no performance degradation reported. Single crystallinity was attributed to its high frequency

operation and light emitting property. In the rest of my thesis, novel applications will be demonstrated to further explore the merits of the NMs.

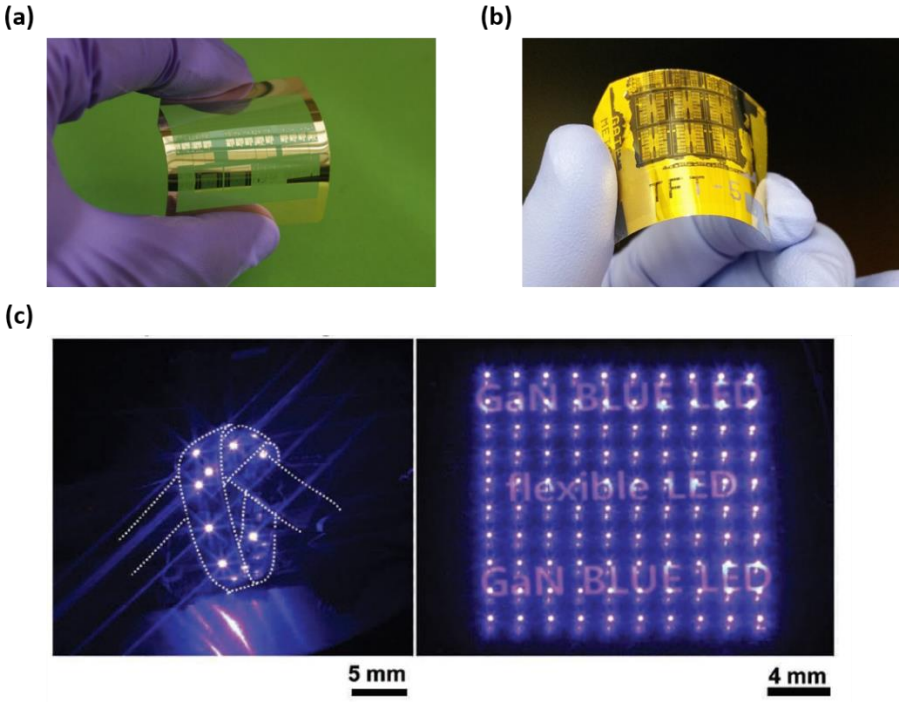

Figure 1.2 *Examples of flexible thin-film electronic and optoelectronic devices:* ***(a)*** *Fast flexible Si NM based transistors with a nanotrench structure.* ***(b)*** *Flexible Si NM based phototransistors.* ***(c)*** *Flexible GaN based light editing diodes.*

1.5 Reference

1 Y. H. Jung*, T.-H Chang*, H. Zhang, C. Yao, Q. Zheng, V. W. Yang, H. Mi, M. Kim, S. J. Cho, D.-W. Park, H. Jiang, J. Lee, Y. Qiu, Z. Cai, W. Zhou, S. Gong, Z. Ma, "High-performance green flexible electronics based on biodegradable cellulose nanofibril paper", *Nature Communications*, 6, 7170 (2015).

2 J.-H. Seo, J. Li, J. Lee, J. Lin, Hx. Jiang, and Z. Ma, "A Simplified Method of Making Flexible Blue LEDs on a Plastic Substrate", *IEEE Photonics Journal*, 7(2) 8200207 (2015).

3 J.-H. Seo, Y. Zhang, H.-C. Yuan, Y. Wang, W. Zhou, J. Ma, Z. Ma, G. Qin, "Investigation of various mechanical bending strains on characteristics of flexible monocrystalline silicon nanomembrane diodes on a plastic substrate", *Microelectronic Engineering*, 110, 40-43 (2013).

4 H. Zhou*, J.-H. Seo*, D. M. Paskiewicz *, Y. Zhu, P. M. Voyles, W. Zhou, M. G. Lagally, Z. Ma, "Fast flexible electronics with strained silicon nanomembranes", *Scientific Report*, 3, 1291 (2013).

5 G. Qin*, J.-H. Seo*, Y. Zhang*, H. Zhou, W. Zhou, Y. Wang, J. Ma, Z. Ma, "RF Characterization of Gigahertz Flexible Silicon Thin-Film Transistor on Plastic Substrates Under Bending Conditions", *IEEE Electron Device Letters* 34, (2), 262-264 (2013).

6 C. C. Wu, S. D. Theiss, G. Gu, M. H. Lu, J. C. Sturm, S. Wagner, and S. R. Forrest, "Integration of organic LEDs and amorphous Si TFTs onto flexible and lightweight metal foil substrates", *IEEE Electron Device Letters* 18, (12), 609-612 (1997).

7 T. Soderstrom, F.-J. Haug, V. Terrazzoni-Daudrix, and C. Ballif, "Optimization of amorphous silicon thin film solar cells for flexible photovoltaics", *Journal of Applied Physics* 103, 114509 (2008).

8 B. Ebenhoch, S. A.J. Thomson, K. Genevicius, G. Juska, Ifor D.W. Samuel, "Charge carrier mobility of the organic photovoltaic materials PTB7 and $PC_{71}BM$ and its influence on device performance", *Organic Electronics* 22, 62-68 (2015).

9 C. Kim, I. Song, W. Nam, and M. Han, *IEEE Electron Device Letters* 23, (6), 315-317 (2002).

10 J. R. Sanchez-Perez, C. Boztug, F. Chen, F. F. Sudradjat, D. M. Paskiewicz, RB Jacobson, M. G. Lagally, and R. Paiella, "Direct-bandgap light-emitting germanium in tensilely strained nanomembranes", *Proceedings of the National Academy of Sciences of the United States of America* 108, (47), 18893-18898 (2011).

11 W. Zhou and Z. Ma, "Breakthroughs in Photonics 2012: Breakthroughs in Nanomembranes and Nanomembrane Lasers", *IEEE Photonics Journal*, 5, (2), 0700707 (2013).

12 T. Akatsu, C. Deguet, L. Sanchez, F. Allibert, D. Rouchon, T. Signamarcheix, C. Richtarch, A. Boussagol, V. Loup, F. Mazen, J.-M. Hartmann, Y. Campidelli, L. Clavelier, F. Letertre, N. Kernevez, C. Mazure, "Germanium-on-insulator (GeOI) substrates—A novel engineered substrate for future high performance devices", *Materials Science in Semiconductor Processing* 9, 444-448 (2006).

13 K. Zhang, J.-H. Seo, W. Zhou, Z. Ma, "Fast flexible electronics using transferrable silicon nanomembranes", *Journal of Physics D: Applied Physics* 45, 143001 (2012).

14 J.-H. Seo, T. Ling, S. Gong, W. Zhou, L. J. Guo, and Z. Ma, "Fast Flexible Transistors with a Nanotrench Structure", *Scientific Reports* 6, 24771, (2016).

15 J.-H. Seo, K. Zhang, M. Kim, H. Yang, W. Zhou, Z. Ma, "Flexible Phototransistors Based on Single-Crystalline Silicon Nanomembranes", *Advanced Optical Materials* 4, 120-125 (2016)

16 T.-I. Kim, Y. H. Jung, J. Song, D. Kim, Y. Li, H.-S. Kim, I.-S. Song, J. J. Wierer, H. A. Pao, Y. Huang, and J. A. Rogers, "High-Efficiency, Microscale GaN Light-Emitting Diodes and Their Thermal Properties on Unusual Substrates", *Small* 8, (11), 1643-1649 (2012).

Chapter 2. Tunable biaxial in-plane compressive strain in a Si nanomembrane transferred on a polyimide film

2.1 Introduction

In recent years, strained silicon (s-Si) has been widely applied to boost carrier mobility in order to achieve a higher drive current in Si-based field-effect transistors (FETs).[1–5] Such strain engineering has been mostly limited to rigid substrates. However, the use of flexible substrates combined with strain engineering enables applications such as flexible sensors and smart patches.[6,7] Although there have been on-going efforts to manipulate the strain in flexible electronics, achieving s-Si on flexible substrates has been a challenge. With the recent advent of transferrable semiconductor nanomembranes (NMs), strain engineering using NMs has received great attention.[8] For example, Yuan et al. first demonstrated the use of tri-layers of single-crystal Si/SiGe/Si NM to obtain s-Si on a plastic substrate.[9] Zhou et al. further utilized the trilayer Si NM to fabricate flexible RF thin-film transistors (TFTs). They achieved a biaxial tensile strain of 0.35% and an approximately 40% enhancement in electron mobility compared to unstrained devices.[10] Additionally, a unique light-emitting property was obtained from indirect band-gap materials, such as germanium (Ge) NM, by applying biaxial tensile strain.[11] Thus, strain engineering in flexible electronics provides a method to enhance the device performance. However, thus far, strain engineering for flexible electronics usually requires expensive growth equipment, such as a metal organic chemical vapor deposition (MOCVD) system, to grow delicate epitaxial layers.[9,10] Although other methods, such as gas blowing, may also be applicable to flexible substrates, such methods could not yield strain without a use of external forces and using this method only tensile strain can be generated.[11] Therefore, there is a need to develop simpler methods to generate strain

on flexible substrates. In this chapter, we report a simple and viable method to create programmable biaxial compressive strain in the Si NM using the unique thermal property of Kapton® HN film. Namely, according to the manufacturer's data sheet, the Kapton® HN film shrinks when exposed to constant heat due to the residual stress generated in the film during its manufacturing process.[12] The Kapton® HN film's unique thermal property allows for the creation of tunable and programmable compressive strains in the film (e.g., Si NM) attached on the top of the Kapton® HN film through an annealing process. We investigated the correlation between the amount of strain and the annealing temperature using Raman spectroscopy and high resolution X-Ray diffraction (HR-XRD). We also created a numerical model using a COMSOL Multiphysics® simulation software to analyze the strain distribution in Si NM after the complete annealing process.

2.2 Background

As shown in Figure 2.1(b), the mechanism of the strain creation in the Si NMs is explained by the expansion and shrinkage of its substrate (i.e., the Kapton HN film) induced during the complete annealing process (i.e., the heating-annealing-cooling process). This mechanistic model was built upon COMSOL Multiphysics simulation (i.e., assuming zero net change in strain from the heating and cooling processes since the same heating and cooling rates were used.) as well as the experimental data (i.e., the measured compressive strain in the Si NM) discussed in detail below. It was reported from the manufacturer's material data sheet that a 125 μm thick Kapton HN film shrunk 0.25 % and 1.54 % after being annealed at 150℃ for 30 min, and 400℃ for 120 min, respectively.[12] This unique thermal property exhibited by the Kapton HN film leads to the formation of compressive strain in the Si NMs transferred onto the Kapton HN films after the

complete annealing process. As shown in Figure 2.1(a), (1) during the temperature ramp-up stage (i.e., the heating process), the Kapton HN film expands linearly with the annealing temperature because the annealing temperature in this study is set to be below the glass transition temperature of the Kapton HN film (T_g = 360 ~ 410℃) (stage I in Figure 2.1(b)).[12] (2) During the annealing stage when the film is heated at a constant temperature, the Kapton HN film shrinks due to the residual stress present in the Kapton HN film (stage II in Figure 2.1(b)). The higher is the annealing temperature, the more shrinkage occurs, and thus the desired amounts of strain can be programmed by adjusting the annealing temperature. (3) During the temperature ramp-down stage (i.e., the cooling process) (stage III in Figure 2.1(b)), the Kapton HN film shrinks down further. Since the heating rate and cooling rate were controlled to be the same (i.e., 20℃/min), the total amount of expansion experienced by the Kapton HN film during the heating process and the total amount of shrinkage occurred during the cooling process cancels out. Therefore, the dimension of the Kapton HN film after the complete heating-annealing-cooling process becomes smaller than its original dimension purely due to the residual (built-in) stress present in the Kapton HN film generated during its fabrication process.[12] As shown in a Figure 2.1(b), the Kapton HN film experiences compressive stress after being cooled to room temperature (RT) and this compressive stress is naturally transferred to the Si NM layer. Moreover, the amount of shrinkage is dependent on the annealing temperature. Therefore, the amount of compressive strain in the Si NMs can be conveniently regulated by controlling the annealing temperature during the complete annealing process. It should be noted that the SU-8 layer experiences shrinkage after the complete annealing process[13] and this facilitates the formation of the compressive strain in Si NM. The maximum annealing temperature was still lower than the decomposition temperature (i.e., ~380℃) of the SU-8 layer.[13] Thus, the SU-8 layer was intact within the range of annealing temperatures we studied

and it functioned well as an intermediate layer for strain transfer from the Kapton HN film to the Si NM. Figure 2.1(a) contains two microscopic images of the transferred Si NM taken before and after it was annealed at 350℃. No wrinkles or fractures on the strained NM were observed.

2.3 Fabrication Process

Figure 2.1 schematically illustrates the process of the development of biaxial in-plane compressive strain in Si NMs attached on the top of the Kapton HN films. The creation of strained Si NMs began with a thorough cleaning of the silicon-on-insulator (SOI) wafer (with a 200 nm thick top Si (100) layer doped with boron at a concentration of 1.0×10^{15} cm^{-3}) with acetone, IPA, and DI water. After the top Si layer was photolithographically defined, the SOI samples were undercut in a concentrated hydrofluoric acid (HF, 49%) solution as reported elsewhere.[13] Then, the released top Si layer, now called Si NM, was flip-transferred onto a 125 μm thick Kapton HN film coated with an 1 lm thick adhesive layer (Microchem, SU-8 2002). Transferred Si NMs (size: 2×1.5 mm^2) were completely glued to the Kapton HN films by following a UV curing process.[14] The samples were annealed at different temperatures in the vacuum chamber with a nitrogen ambient. During the annealing process, the samples were heated to the set temperature at a heating rate of 20℃/min and annealed for 20 min. Then, the samples were cooled down to RT (25℃) at a cooling rate of 20℃/min. To investigate the effects of annealing temperatures on the amount of strain that can be generated, three annealing temperatures, namely, 100, 200, and 350℃, were chosen for this study. Raman spectroscopy (Horiba micro-Raman spectroscopy with a 532nm wavelength laser) was used to evaluate the biaxial in-plane compressive strain in the Si NMs annealed at different temperatures. Ten areas (size: 6×6 μm^2) on the samples annealed at different temperatures, including 100, 200, and 350℃, were randomly chosen for the characterization of in-

plane compressive biaxial strains. The Si NMs were annealed for 1, 5, 10, and 20 min at 350℃ to establish the correlation between the induced compressive strain and the annealing time. The electrical current changes of the annealed Si NMs associated with their strain changes were also characterized. Raman mapping on a 100 × 100 μm^2 area was also performed to analyze the strain distribution. X-ray diffraction (XRD, PANalytical X'Pert PRO X-ray diffractometer) analyses were carried out for the Si NM annealed at 350℃ to evaluate the out-of-plane (perpendicular to the Si NM) strain, created by the in-plane stress. A $\theta/2\theta$ scan was taken around the (004) reflection to obtain the out-of-plane strain of the Si NM (Cu, Ka: 0.154 nm wavelength). Furthermore, in order to analyze the strain distribution in the Si NM, numerical simulations of the three-dimensional (3-D) deformation of the Si NM on the Kapton HN film were carried out by COMSOL Multiphysics.

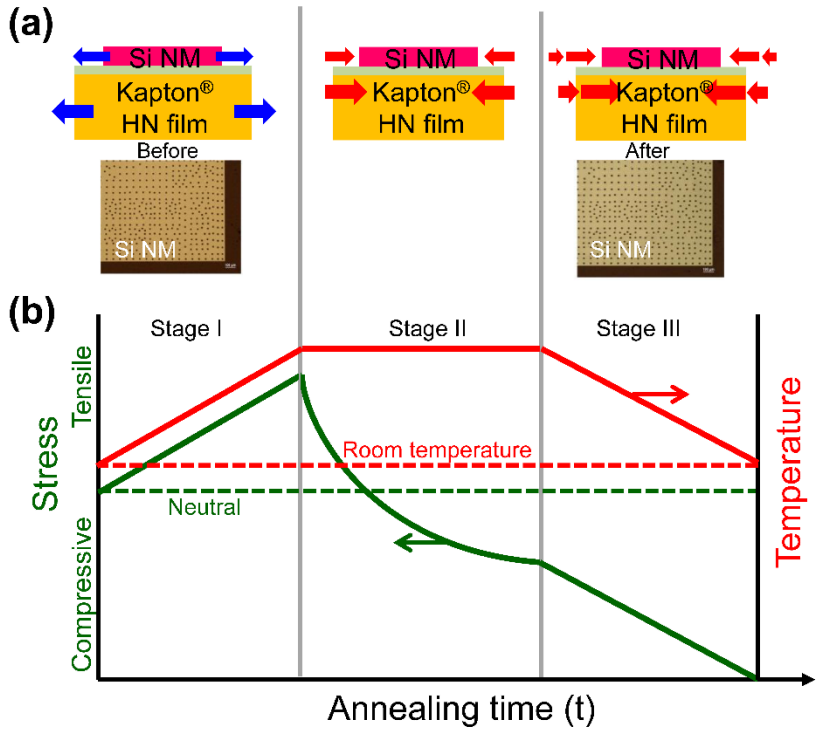

Figure 2.1. (a) *Schematic illustration of the mechanism for the creation of the programmable biaxial compressive strain in a Si NM on a Kapton HN film using the thermal annealing process. During the heating process (stage I), transferred Si NM is under a tensile stress due to the expansion of the Kapton HN film (stage I). During the annealing process (stage II), the tensile stress in the Si NM is decreased consistently resulting from the shrinkage of the Kapton HN film caused by the residual stress present in the Kapton HN film (stage II). During the cooling process (stage III), the Si NM is subjected to a compressive stress caused by the additional shrinkage of the Kapton HN film (stage III). Insets are the microscopic images of the transferred Si NM on a Kapton HN film before and after annealing at 350℃.* ***(b)*** *The stress profiles as a function of time, along with temperature profile, to show the change of stress during the complete annealing process.*

2.4 Experimental Results and Discussion

Figure 2.2(a) shows the typical Raman spectra of the as-transferred Si NM (i.e., without any external strains) as well as the Si NM after it was annealed at 350℃ for 20 min. The Raman scattering peak of the Si-Si vibration modes for the as-transferred Si NM appeared at 520.1 cm^{-1}. The Raman peak of the annealed Si NM was shifted to a larger wavenumber by 4.2 cm^{-1} compared to that of the as-transferred Si NM, indicating that a compressive strain was induced by the complete annealing process.

The biaxial stress value in the Si NM can be extracted according to the Raman shift using the following equation:

$$\sigma_{xx} + \sigma_{yy}(MPa) = -434 \times \Delta\omega(cm^{-1}) \qquad (1)$$

where σ_{xx} and σ_{yy} are biaxial stress along the in-plane horizontal (x) and longitudinal (y) directions, respectively, and $\Delta\omega$ is the Raman peak shift. The proportional constant for Si used in Eq. (1) was calculated based on the phonon deformation potentials of Si.[15] Because the Kapton HN film has the same amount of thermal shrinkage along the x and y directions, Eq. (1) can be re-written as

$$\sigma_{xx} + \sigma_{yy}(MPa) = -434 \times \Delta\omega(cm^{-1}) \qquad (2)$$

The corresponding strain in the Si NM can be calculated based on the relationship among the stress (σ), strain ($\varepsilon=\sigma/E$), and Young's modulus for Si ($E_{[110]}$=169 GPa)[16]

$$\varepsilon_{xx}(\%) = \varepsilon_{yy}(\%) = -0.128 \times \Delta\omega(cm^{-1}) \qquad (3)$$

Using Eqs. (1) – (3), the biaxial strains of 0.11%, 0.16%, and 0.54% in the Si NM were calculated from the samples annealed at 100, 200, and 350℃, respectively. Figure 2.2(b) shows the typical Raman peak shifts taken from 10 small areas (6 × 6 μm^2) on the Si NMs annealed at 100, 200, and 350℃, respectively. Figure 2.2(b) shows that the induced biaxial compressive strains increased sharply against the annealing temperatures. This behavior could be attributed to the different amount of shrinkage experienced by the Kapton HN film at different annealing temperatures.

In order to establish the correlation between the induced compressive strain and the annealing time, Raman analysis was carried out on the samples (Kapton HN film/SU-8/Si NM stack) annealed for 1, 5, 10, and 20 min at 350℃. Figure 2.2(c) shows the Raman peak shift and the corresponding strain in the Si NM annealed at 350℃ at four different annealing times. The Raman peak shifts corresponding to 1, 5, 10, and 20 min annealing time were measured to be 2.28, 4.2, 4.2, and 4.2 cm^{-1}, which was converted to a compressive strain value of 0.29 %, 0.54 %, 0.54 %, and 0.54 %, respectively. Namely, according to the Raman shifts, the compressive strain

reached a plateau of 0.54 % within the first 5 min of the annealing process. These results indicate that the strain was induced within a short period of time during the annealing process and no strain relaxation in the Si NM was observed after 20 min annealing.

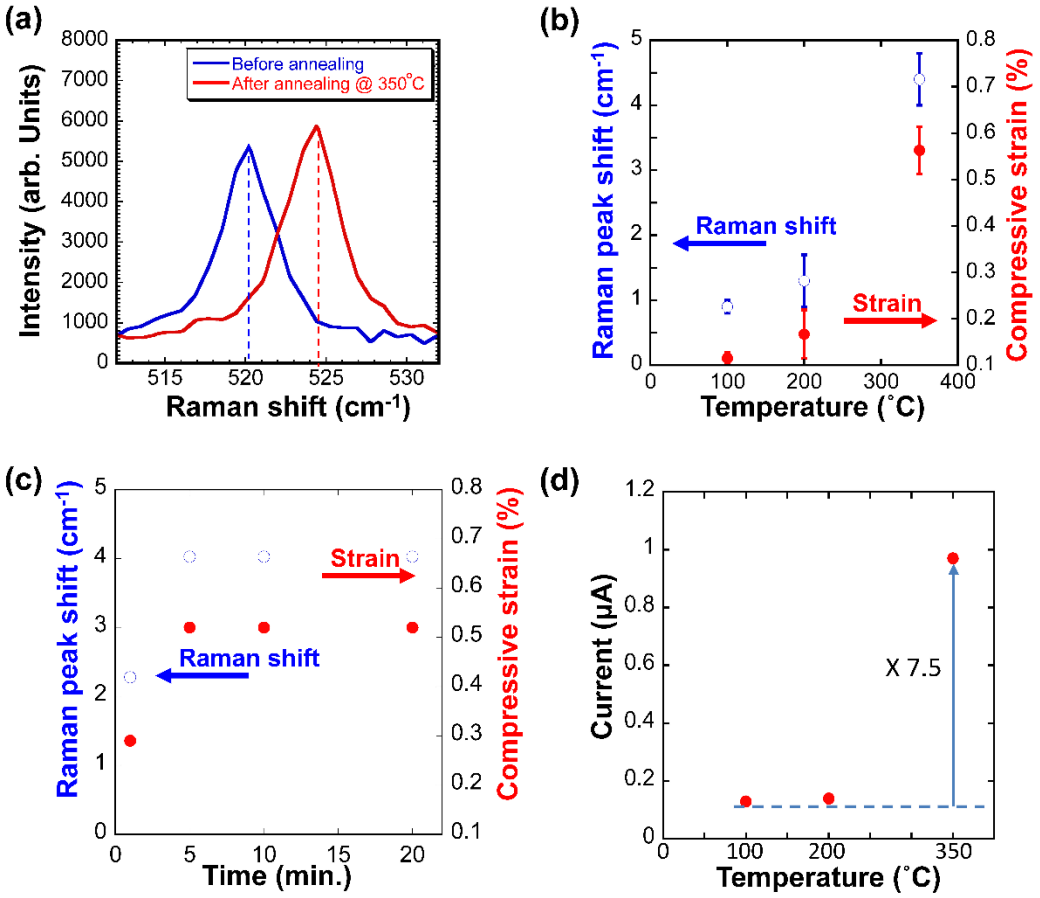

Figure 2.2. (a) *Raman spectra for the Si NM before and after being annealed at 350 ℃ for 20 min.* ***(b)*** *Raman peak shift (cm^{-1}) and strain (%) in the Si NM with respect to the annealing temperature (℃).* ***(c)*** *Raman peak shift (cm^{-1}) and strain (%) in the Si NM annealed at 350 ℃ with respect to the annealing time (min).* ***(d)*** *Current (μA) measured at 2 V between two metal electrodes on the Si NMs annealed at 100 ℃, 200 ℃, and 350 ℃.*

In order to determine the correlationship between the current changes and the magnitude of induced strains, two metal electrodes (Ti/Au= 20/130 nm) that were 30 μm apart were deposited

onto the surface of the strained Si NM by e-beam evaporation. Figure 2.2(d) shows the currents measured at 2 V between the two metal electrodes for samples annealed at various temperatures. While the current changes were rather small for the samples annealed at 100℃ (0.13 μA) and 200℃ (0.14 μA), respectively, a significant current increment was observed for the sample annealed at 350℃ (0.97 μA). As demonstrated in Figure 2.2(b) and 2.2(d), the correlation between the current increase and the annealing temperature was similar to the correlation between the induced strain and the annealing temperatures. The increase in current at high annealing temperatures could be attributed to the fact that the conduction band of Si was split into two valleys due to the presence of induced strain which consequently increased the hole mobility. Based on the calculation of the hole mobility in biaxially strained Si,[17] an approximately 50% increase in the hole mobility is expected. These results confirmed a strong correlation between the current increase and the induced strain.

Figure 2.3 shows that the XRD peak of Si NMs was shifted to a smaller angle after the completion of the annealing process (i.e., 350℃). To extract the out-of-plane strain value of the Si NM from the measured XRD data, the lattice spacing needs to be calculated. Because in-plane compressive stress existed in the annealed Si NM, the lattice spacing perpendicular to the Si NM increased as the XRD peak shifted to a smaller diffraction angle. The lattice spacing normal to the top surface of the Si NM can be calculated by Bragg's law:[18]

$$a = \frac{\lambda}{2 \times \sin\theta} \times \sqrt{\left(h^2 + k^2 + l^2\right)} \qquad (4)$$

where *a* is the lattice spacing, *k* is the X-ray wavelength, *h* is the diffraction angle, and *(hkl)* is the diffraction plane. While the full width at half maximum (FWHM) values remained the same at ~0.04°, the diffraction angle of Si NM was shifted from 34.78° to 34.64° after the NM was annealed

at 350℃ for 20 min. Accordingly, the change in lattice spacing (Δa) was calculated to be 0.01908 Å according to Eq. (4). The strain corresponding to the lattice space change can be expressed as:

$$\varepsilon = \frac{\Delta a}{a} \qquad (5)$$

Based on the above equations and measurements, the tensile strain perpendicular to the Si NM was determined to be 0.35 %. It should be noted that this strain value calculated from the XRD data refers to the out-of-plane strain (i.e., perpendicular to the surface), whereas the strain value of 0.54 % calculated from the Raman spectrum refers to the in-plane strain (i.e., parallel to the surface).

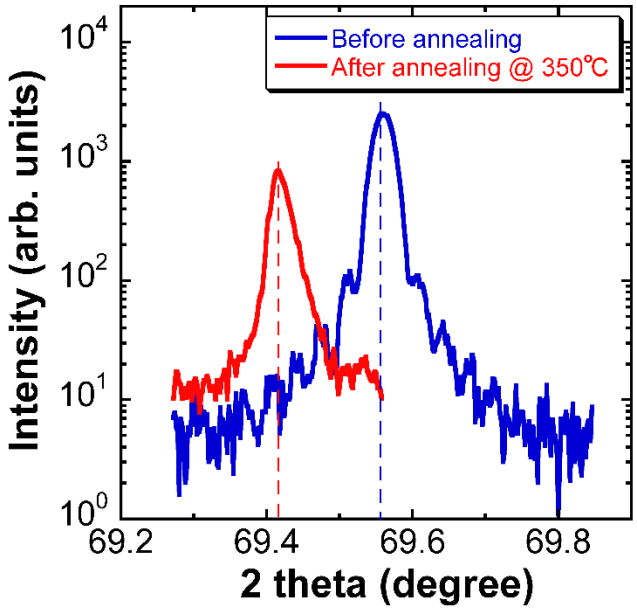

Figure 2.3. *X-ray diffraction (XRD) θ/2θ spectra for the as-transferred Si NM (blue) and the Si NM after being annealed at 350℃ for 20 min (red).*

In order to fully characterize the uniformity of its strain distribution in the Si NM annealed at 350℃, a 100 × 100 μm^2 area was scanned with a resolution of about 6 × 6 μm^2 for the sample. Figure 2.4(a) and 2.4(b) show the Raman mapping and its corresponding Raman peaks. The highest Raman peak shift observed from area (iii) was 3.97 cm^{-1} and the lowest one from area (i)

was 1.75 cm^{-1}. In particular, the Raman peaks of the Si-Si vibrational modes of area (i), (ii), and (iii) were measured at 521.85, 523.18, and 524.3 cm^{-1} which corresponded to the strain of 0.22 %, 0.39 %, and 0.54 %, respectively. The four etched holes in the Si NM appeared as four white squares, due to the absence of Si. Although there were some minor color difference right next to the etched holes in the Raman map (referred to as the edge effect), most areas exhibit brown color. The brown color in the Raman map of the scanned areas represents the Raman peaks with a value around 524 cm^{-1}. The measured strain values of most areas were calculated to be 0.4 % ~ 0.5 %. This uniform color distribution in the Raman map indicates that the strain was evenly distributed over a large area with a minor edge effect. A static strain simulation was carried out by COMSOL Multiphysics with a solid stress strain model of structure mechanics to evaluate the strain distribution. Vertically stacked films of Si NM/SU-8/Kapton HN film with a surface size of 100 × 100 μm^2 and containing four etched holes was used. The thicknesses of the Si NM, SU-8, and Kapton HN film used in the modeling were 200 nm, 1 μm, and 125 μm, respectively, which was the same with the dimensions of the samples used for the measurements. For the Si NM, Young's modulus of 169 GPa, Poisson's ratio of 0.27, and mass density of 2330 kg/m3 were taken from literature.[19,20] Young's modulus of 2.3 and 2.5 GPa, Poisson's ratio of 0.26 and 0.34, and mass density of 1190 and 1420 kg/m3 were used for SU- 8 and Kapton HN film, respectively.[12,21,22] Based on the experimental results (i.e., the biaxial compressive strain of 0.54 % in the Si NM was induced by the annealing at 350℃), a 0.54 % of shrinkage was applied on the Si NM along the x and y directions, respectively, in the simulation. Figure 2.4(c) shows the simulation result of the strain distribution in the Si NM. The uniform blue color indicates that the strain was evenly distributed in most part of the Si NM; however, there was a minor edge effect around the etched holes, which is consistent with the Raman map. Figure 2.4(d) plots the simulated strain values of

the two cross-sections along a horizontal direction. The first line (line I) scans the center of the Si NM and the second line (line II) scans the regions close to the edges of the etched holes (i.e., 2 μm above the edges). As shown in the first line scan, the strain near the edges of the 100 × 100 μm^2 Si NM was approximately 0.05 % lower than the central area. The second scan shows that the strain values slightly decreased (~0.03 %) at the edges of the etched holes. Overall, the simulated strain distribution agreed well with the experimental results deduced by Raman mapping, namely, the compressive strain in the Si NM was rather uniform except the minor edge effect. For the Raman map shown in Figure 2.4(a), the minor edge effect was only observed at areas surrounding the etched holes, but not around the edges of the scanned region (i.e., 100 × 100 μm^2) because the scanned Si NM was a part of the large transferred Si NM.

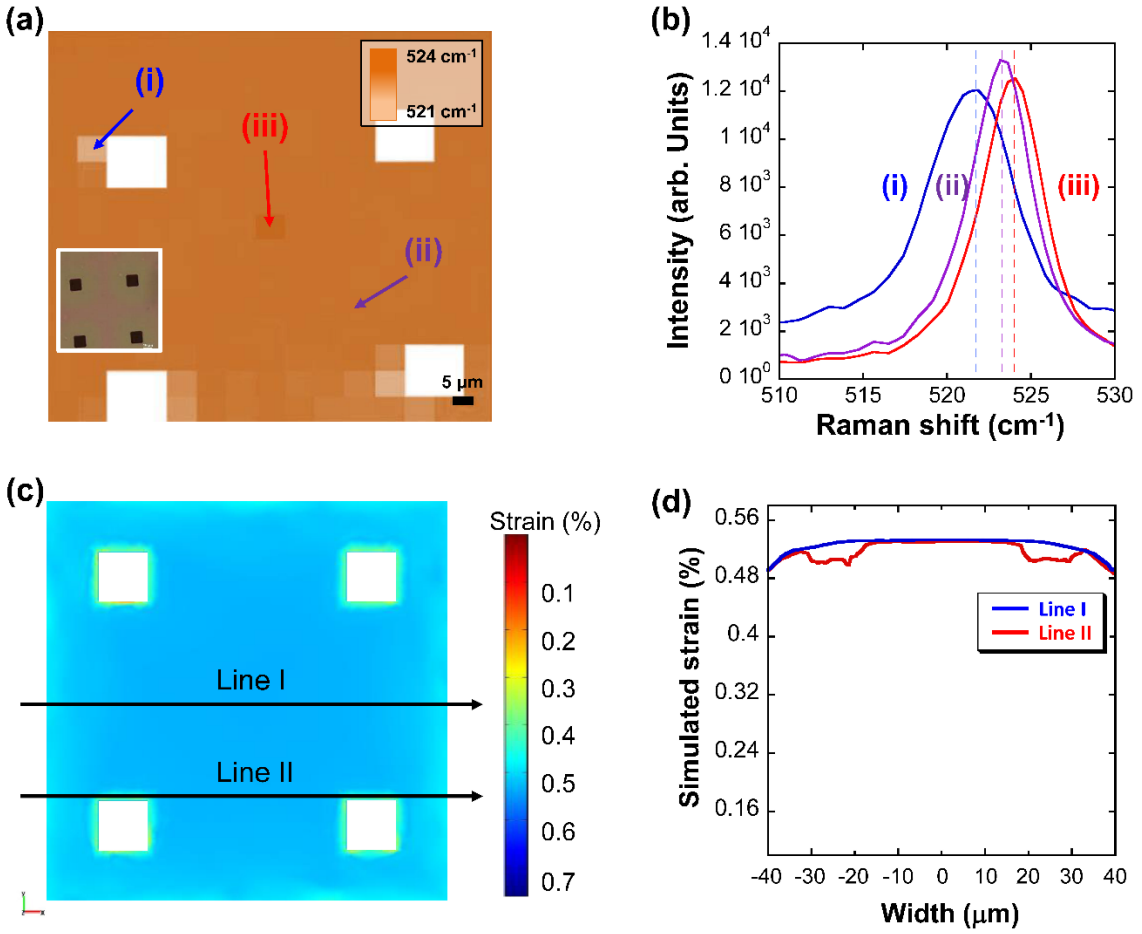

Figure 2.4. (a) *Raman map covering a 100 × 100 μm^2 size after being annealed at 350℃. The size of each square area is 6 × 6 μm^2. Inset is the microscopic image of the scanned area.* ***(b)*** *Raman peak shifts, corresponding to the areas (6 × 6 μm^2) labeled as (i)–(iii) in (a). Simulated biaxial compressive strain in the Si NM transferred onto the Kapton HN film by COMSOL Multiphysics after the complete annealing process (350℃ for 20min).* ***(c)*** *The simulated strain distribution in the Si NM transferred on the Kapton HN film.* ***(d)*** *The simulated strain values scanned along the lines I and II.*

2.5 Conclusion

In summary, a simple and viable method to create programmable biaxial in-plane compressive strain in Si NM was developed using the unique thermal characteristic of the Kapton HN film. According to the Raman spectroscopy and COMSOL Multiphysics simulation, the compressive strain created in the Si NM was distributed uniformly across the NM except the minor edge effect. Within the range of annealing temperatures studied (from 100 to 350℃), the amount of compressive strain created in the Si NM increased with the annealing temperatures. For instance, 0.11 % and 0.54 % compressive strain were generated in the Si NM at an annealing temperature of 100 and 350℃, respectively. Thus, this method provides a viable approach to produce in-plane compressive strain in NMs for various applications.

2.6 Reference

1 J. Suh, R. Nakane, N. Taoka, M. Takenaka, and S. Takagi, "Highly strained-SiGe-on-insulator p-channel metal-oxide-semiconductor field-effective transistors fabricated by applying Ge condensation technique to strained-Si-on-insulator substrates", Appl. Phys.Lett. 99, 142108 (2011).

2 K. Ghosh, S. Das, A. Fissel, H. J. Osten, and A. Laha, "Epitaxial Gd_2O_3 on strained $Si_{1-x}Ge_x$ layers for next generation complementary metal oxide semiconductor device application", Appl. Phys. Lett.103, 153501 (2013).

3 S. Suthram, P. Majhi, G. Sun, P. Kalra, H. R. Harris, K. J. Choi, D. Heh, J. Oh, D. Kelly, R. Choi et al., "High Performance pMOSFETs Using Si/Si1-xGex/Si Quantum Wells with High-k/Metal Gate Stacks and Additive Uniaxial Strain for 22 nm Technology Node", IEDM Tech. Dig. 2007, 727–730.

4 J.-P. Han, H. Utomo, L. W. Teo, N. Rovedo, Z. Luo, R. Krishnasamy, R. Stierstorfer, Y. F. Chong, S. Fang, H. Ng et al., "Novel Enhanced Stressor with Graded Embedded SiGe Source/Drain for High Performance CMOS Devices", IEDM Tech. Dig. 2006, 1–4.

5 T. Ghani, M. Armstrong, C. Auth, M. Bost, P. Charvat, G. Glass, T. Hoffiann, K. Johnson, C. Kenyon, J. Klaus et al., "A 90nm high volume manufacturing logic technology featuring novel 45nm gate length strained silicon CMOS transistors", IEDM Tech. Dig. 2003, 11.6.1–11.6.3.

6 M. Segev-Bar and H. Haick, "Flexible Sensors Based on Nanoparticles", ACS Nano 7(10), 8366–8378 (2013).

7 M. Segev Bar, G. Konvalina, and H. Haick, "High-Resolution Unpixelated Smart Patches with Antiparallel Thickness Gradients of Nanoparticles", Adv. Mater. 27, 1779–1784 (2015).

8 M. M. Roberts, L. J. Klein, D. E. Savage, K. A. Slinker, M. Friesen, Ge. Celler, M. A. Eriksson, and M. G. Lagally, "Elastically relaxed free-standing strained-silicon nanomembranes", Nat. Mater. 5, 388–393 (2006).

9 H.-C. Yuan, Z. Ma, M. M. Roberts, D. E. Savage, and M. G. Lagally, "High-speed strained-single-crystal-silicon thin-film transistors on flexible polymers", J. Appl. Phys. 100, 013708 (2006).

10 H. Zhou, J.-H. Seo, D. M. Paskiewicz, Y. Zhu, G. K. Celler, P. M. Voyles, W. Zhou, M. G. Lagally, and Z. Ma, "Fast flexible electronics with strained silicon nanomembranes", Sci. Rep. 3, 1291 (2013).

11 J. R. Sanchez-Perez, C. Boztug, F. Chen, F. F. Sudradjat, D. M. Paskiewicz, R. B. Jacobson, M. G. Lagally, and R. Paiella, "Direct-bandgap light-emitting germanium in tensilely strained nanomembranes", Proc. Natl. Acad. Sci. U. S. A. 108(47), 18893–18898 (2011).

12 See http://www2.dupont.com/Kapton/en_US/assets/downloads/pdf/HN_datasheet.pdf, for Physical properties and dimensional stability of HN Kapton film.

13 W. Zhou, D. Zhao, Y.-C. Shuai, H. Yang, S. Chuwongin, A. Chadha, J.-H. Seo, K. X. Wang, V. Liu, Z. Ma, and S. Fan, "Progress in 2D photonic crystal Fano resonance photonics", Prog. Quantum. Electron. 38(1), 1–74 (2014).

14 R. Feng and R. J. Farris, "Influence of processing conditions on the thermal and mechanical properties of SU8 negative photoresist coatings", J. Micromech. Microeng. 13, 80–88 (2003).

15 E. Anastassakis, A. Canterero, and M. Cardona, "Piezo-Raman measurements and anharmonic parameters in silicon and diamond", Phys. Rev. B 41, 7529–7535 (1990).

16 C. Himcinschi, M. Reiche, R. Scholz, S. H. Christiansen, and U. Gosele, "Compressive uniaxially strained silicon on insulator by prestrained wafer bonding and layer transfer", Appl. Phys. Lett. 90, 231909 (2007).

17 D. Yu, Y. Zhang, and F. Liu, "First-principles study of electronic properties of biaxially strained silicon: Effects on charge carrier mobility", Phys. Rev. B 78, 245204 (2008).

18 C. Kittel and P. McEuen, Introduction to Solid State Physics, 8th ed. (John Wiley & Sons. Inc., 2004).

19 J. J. Wortman and R. A. Evans, "Young's Modulus, Shear Modulus, and Poisson's Ratio in Silicon and Germanium", J. Appl. Phys. 36, 153 (1965).

20 L. B. Freund and S. Suresh, Thin Film Materials: Stress, Defect Formation, and Surface Evolution (Cambridge University Press, Cambridge, UK; New York, 2003).

21 S. Keller, G. Blagoi, M. Lillemose, D. Haefliger, and A. Boisen, "Processing of thin SU-8 films ", J. Micromech. Microeng. 18, 125020 (2008).

22 I. Roch, P. Bidaud, D. Collard, and L. Buchaillot, "Fabrication and characterization of an SU-8 gripper actuated by a shape memory alloy thin film", J. Micromech. Microeng. 13, 330–336 (2003).

Chapter 3. Resonant tunneling in multiple barrier heterostructures formed by single crystalline Si nanomembranes and amorphous aluminum oxide

3.1 Introduction

QWs consist of ultrathin semiconductor layers (i.e., semiconductor wells) sandwiched by barrier layers from which we can observe special properties by the quantum confinement of charge carriers.[1,2] These layers, in which both electrons and holes are confined, are typically very thin (10 nm or less) and of high quality to confine excitons (electrons and holes), as well as to avoid unwanted recombination sites.[3] For these reasons, the formation of QWs has been realized by high-precision epitaxial growth techniques such as metal-organic chemical vapor deposition (MOCVD) or molecular beam epitaxy (MBE).[4,5] Although such techniques have been widely and successfully used to realize many modern electronic devices, one significant restriction to the choice of material combination is that the lattice constants of the materials for the "walls" and "barriers" should be identical or at least very similar.[6] If two materials have significantly different lattice constants, the crystal structure will have a large number of defects and will not be an epitaxial layer anymore. Therefore, only a few of the material combinations are applicable to form a QW structure such as Si/SiGe[7,8] and AlGaAs/GaAs.[9,10] From the aspect of practical applications, creating QW on Si substrates implies direct integration of optoelectronics and photonics with Si CMOS. Furthermore, deep QWs with large spread quantized energy levels allow RT operation of on-Si optoelectronic components. However, the QW structures epitaxially grown suffer from limited well depth and thus a limited number of quantized energy levels due to a relatively small band offset (i.e., available barrier height).

Semiconductor-oxide structured QWs have been theoretically predicted to offer a larger band offset (i.e., larger barrier height) than the aforementioned conventional (from epitaxy) QW structures, and thus enhances quantum confinement and enables larger freedom of manipulation of the band structures.[11,12] Such deep QW structure is expected to offer stronger resonant tunneling and NDR due to the high mobility of single crystalline well materials.[13] However, such structures have not been realized due to the difficulty to form single crystalline films on top of amorphous oxide materials. Up until recently, most of the semiconductor-oxide QWs still rely on epitaxial growth techniques and single crystalline-amorphous oxide structures were not yet possible.[14,15] Recently, alternative methods such as wafer bonding were used to create semiconductor-oxide QWs, but it could only demonstrate a single QW structure due to a process limitation.[16] Moreover, a QW structure that was formed by the wafer bonding process does not have provided well/barrier sharpness of energy due to a slow atomic transition between a semiconductor and an oxide by a poor passivation associated with a native oxide.[17]

In this paper, we report the demonstration of multiple barrier heterostructures (MBHs) formed by stacking transferable Si nanomembrane (NM) as a well layer and depositing amorphous Al_2O_3 as barrier layer. Recent advances in NM transfer technique allow single crystalline NMs to be transfer-printed onto a new host substrate with an extremely clean interface.[18,19] Si NMs not only inherit the single crystalline quality and the electronic properties of bulk Si wafer,[20] but also enable to form a multi-QW structure by multiple transfer steps which were impossible to realize by other alternative bonding methods. The Al_2O_3 layer coated by an ALD system is known as one of the best materials to passivate the Si surface,[21] thus reducing the unwanted recombination sites effectively and enabling a sharp potential well. As a proof-of-concept demonstration using this approach, we have fabricated RTDs with single QW (double barrier: DB) and double QWs (triple

barrier: TB) on a Si substrate and successfully have observed the quantum tunneling effects at RT. A distinct quantum confinement in the Al_2O_3/Si NM RTD exhibited a NDR with high peak-to-valley ratio at RT, which was predicted only theoretically before.[13] In order to analyze the band offset between Si NM and Al_2O_3 and the strain of transferred Si NM, X-ray photoelectron spectroscopy (XPS, Thermo Scientific K-alpha XPS) and Raman spectroscopy (Horiba LabRAM ARAMIS) were performed. The surface morphologies of the thinned and transferred Si NMs were analyzed by atomic force microscopy (AFM, Park Systems). Finally, the Al_2O_3/Si/Al_2O_3/Si/Al_2O_3 MBH was investigated using high resolution transmission electron microscopy (HR-TEM, Tecnai TF-30).

3.2 Fabrication Process

Figure 3.1(a) schematically illustrates the representative processing steps for fabricating the Al_2O_3/Si /Al_2O_3 DB and TB heterostructures. A 200 nm thick top Si layer on a silicon-on-insulator (SOI) wafer was thinned down to 30 nm using dry oxidation. The thinned top Si, now called Si NM, was then released in concentrated hydrofluoric acid (HF, 49%) (Figure 3.1(a) a1-a4). The Si NM was transfer-printed (stacked) to Al_2O_3 (3 nm)-coated, i-n^+ Si substrate via elastomeric stamp (Figure 3.1(a) b1-b2),[22] followed by rapid thermal annealing (RTA) to enhance the bonding strength. Then, the stacked Si NM was further thinned down to 10 nm by reactive ion etching (RIE) (Figure 3.1(a) b3). The second Al_2O_3 layer (3 nm) was deposited and i-n^+ Si NM (released from another SOI) was transfer-printed on top to complete the DB structure (Figure 3.1(a) b4-c1). For the TB structures, we repeated one more step of the Al_2O_3 deposition and transfer-printing of thinned Si NM. After the deposition of plasma enhanced chemical vapor deposition (PECVD) SiO_2 to passivate devices and opening vias, the anode and cathode were deposited

(Figure 3.1(a) c2). Figure 3.1(b) and (c) show the layer structure and the band-diagram of the DB and TB RTDs in a state of equilibrium. It should be noted that the intrinsic (*i*) Si layer on top of the substrate was grown by MBE at ultra-high vacuum in order to reduce impurity scattering of travelling electrons during device operation and the partially n^+ doped layer on the top part of the *i* Si NM was formed by the ion-implantation process to make an ohmic contact.

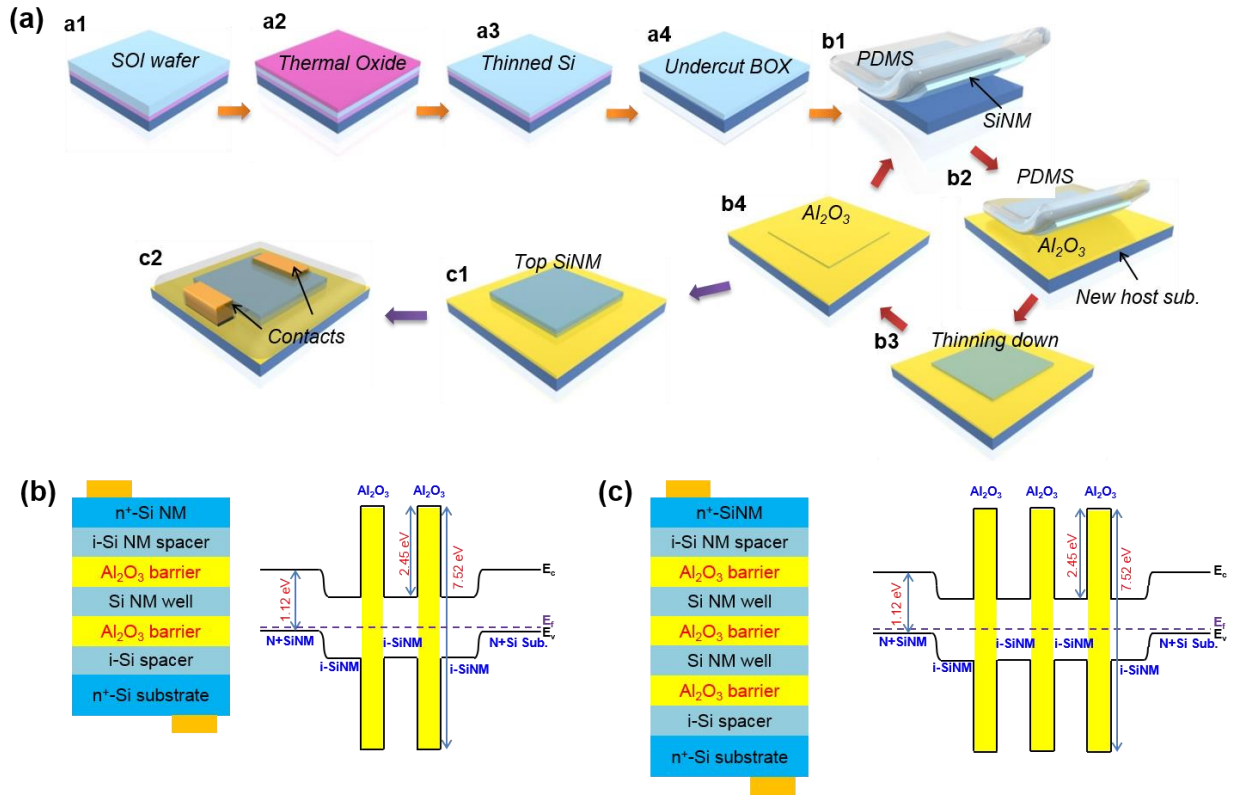

Figure 3.1. *Fabrication processes and detailed layer structures of Si NM/Al_2O_3 RTDs:* ***(a)*** *An illustration of the fabrication steps. a1. Fabrication begins with cleaning a SOI wafer. a2. Dry oxidation to consume the top Si layer. a3. Remove the oxidized top layer by HF to thin the top Si layer down to a 30 nm. a4. Selective wet etching of a BOX layer by HF to release a top Si layer. b1. Gently pick up a Si NM by a PDMS stamp b2. The transfer-printed Si NM on a 3 nm Al_2O_3 deposited n^+ Si host substrate. b3. Anneal at 300℃ to enhance the bond strength, followed by dry*

etching to further thin down the transferred Si NM to 10 nm. b4. Deposit a 3 nm Al_2O_3 layer. For the triple barrier structures, repeat steps b1-b4 to form an additional pair of Si NM/Al_2O_3 quantum wells. c1. Transfer an intrinsic/phosphorus doped Si NM and anneal. c2. Deposit a 200 nm SiO_2 layer and etch via to fill the Ti/Au anode and cathode. Layer structures and band diagrams at the equilibrium state for ***(b)*** *Si NM/Al_2O_3 double and* ***(c)*** *triple barrier RTDs are shown.*

3.3 Experimental Results and Discussion

Figure 3.2(a) shows a microscopic image of an array of Si NM (10 nm thick, 120 × 120 μm^2 size) transferred onto an *i*-n^+ substrate. The transferred 10 nm thick thinned Si NMs were nearly transparent due to its thinness. Figure 3.2(b) shows the microscopic image of TB structures after the completion of the stacking of three Si NMs where the top *i*-n^+ Si NMs are shown in blue. It should be noted that an atomically smooth interface is critical to realizing the quantum confinement between barriers and thus to obtaining NDR in RTD at RT.[23] Therefore, careful control of surface roughness during the Si NM thinning process was required. Typical AFM images of the Si NMs before and after the thinning process are shown in Figure 3.2(d) and (f), respectively, indicating that no fractures or cracks on the Si NMs were found during the thinning and transfer-printing processes. As shown in Figure 3.2(d), the thickness of Si NM after the first thinning (from 200 nm to 30 nm) and transfer steps was measured to be 33.12 nm with the root mean square (RMS) roughness (R_q) of 1.425 nm. Figure 3.2(f) shows a 3 dimensional (3D) AFM image and its surface profile after the second thinning step (from 30 nm down to 10 nm). The thickness and R_q of the final Si NM were measured to be 12.52 nm and 0.861 nm, respectively. The improvement of the surface roughness of R_q from 1.425 to 0.861 nm by the second thinning

step (i.e., the RIE etching step) can be explained by the volatile etching of by-products, particularly when the rough surface is preexisted.[24,25]

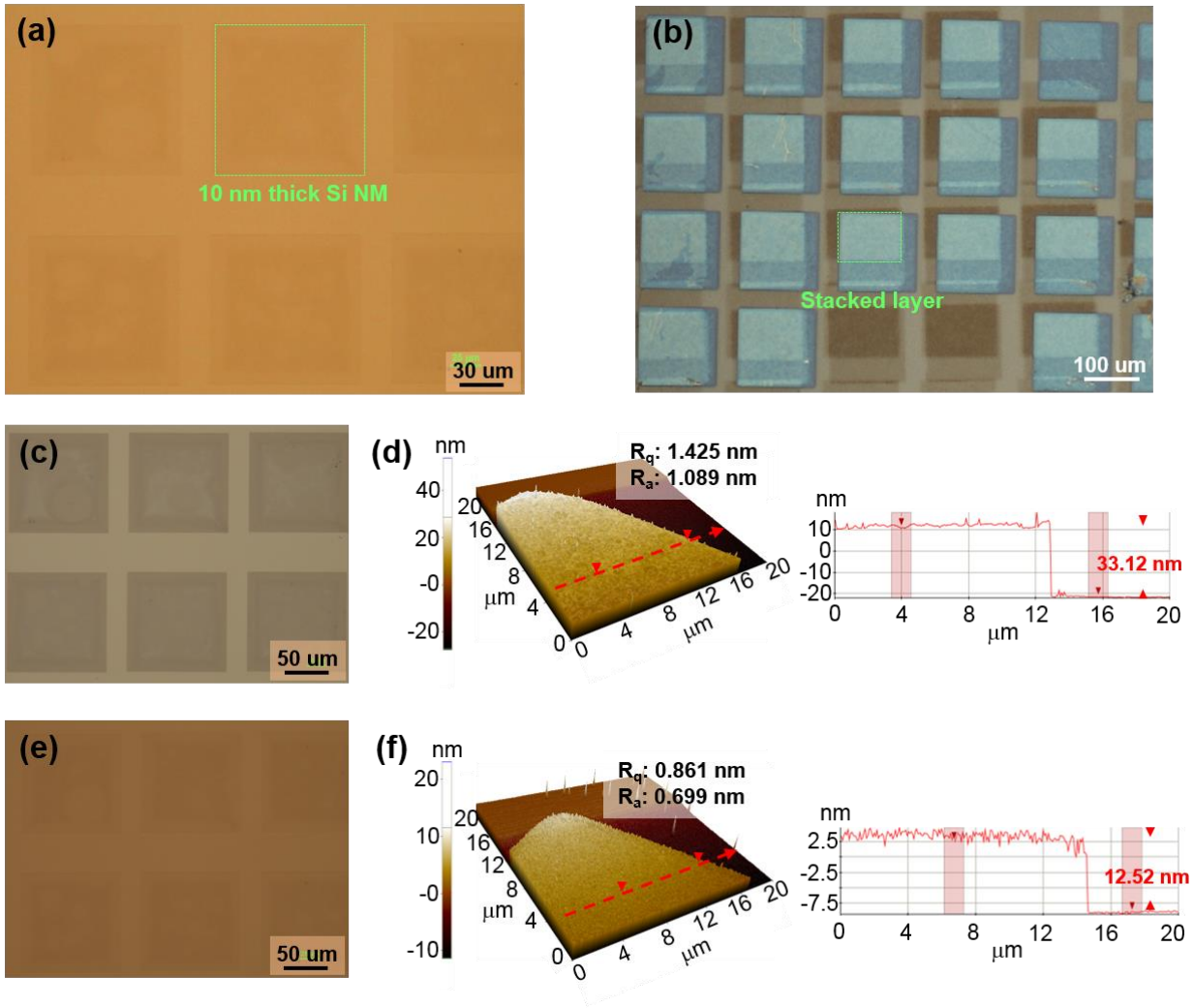

Figure 3.2. *Interface analysis of transferred ultrathin Si NM and Al_2O_3:* ***(a)*** *Microscopic image of thinned Si NMs to 10 nm and transfer-printed onto an Al_2O_3 coated n^+ Si substrate corresponding to the processing step shown in Figure 3.1 (b3).* ***(b)*** *Microscopic image of transfer-printed Si NM/Al_2O_3/Si NM/Al_2O_3/Si NM/Al_2O_3/Si substrate.* ***(c)*** *Microscopic image of a transfer-printed 30 nm thick Si NM.* ***(d)*** *3D AFM image of transferred 30 nm thick Si NM on an Al_2O_3 coated Si host substrate and surface profile shown by AFM scanning along the direction of the red arrow.* ***(e)***

Microscopic image of 10 nm thick Si NMs. ***(f)*** *3D AFM image of transferred 10 nm thick Si NM on an Al_2O_3 coated Si host substrate and surface profile shown by AFM scanning along with the red arrow direction showing uniform thickness with roughness of 0.699 nm.*

To experimentally determine the valence and conduction band discontinuities at Al_2O_3/Si NM heterojunction, XPS analysis was carried out. The measurement was performed on the identical structure with the same thickness (i.e., 3 nm Al_2O_3/10 nm Si NM) using a micro-focused monochromatic Al Ka X-ray source. Figure 3.3(a) shows a typical XPS spectrum collected from the 3 nm Al_2O_3/10 nm Si NM sample. Peak centroids of Si2p and Al2p were measured to be 99.08 eV and 74.78 eV, respectively. The energy difference between the valence band edge and the Al2p centroid of the Al_2O_3 was evaluated from the sample with a thicker Al_2O_3 (10 nm Al_2O_3/Si). The valence band edge of the Al_2O_3 was extracted to be 4.55 eV using the regression-determined line segment (See Figure 3.4(a)).[26] The energy difference between the valence band edge and the Al2p centroid was calculated to be 70.73 eV using the measured peak centroid of the Al2p (i.e., 75.28 eV). Based on the above measurements, the valence and conduction band offset can be determined using the following equation[27]

$$\Delta E_V = \left(E_{Si2p} - E_{Al2p}\right)_{Si/Al_2O_3} - \left(E_{Si2p} - E_V\right)_{Si} + \left(E_{Al2p} - E_V\right)_{Al_2O_3} \qquad (1)$$

$$\Delta E_C = \Delta E_V - \left(\Delta E_g\right)_{SiNM-Al_2O_3} \qquad (2)$$

where E_V is the valence band edge and $(\Delta E_g)_{Si\ NM\text{-}Al2O3}$ is the band gap difference between the Si NM and Al_2O_3. The valence band offset was determined to be -3.95 eV. To evaluate the conduction band offset, the band gap of the Al_2O_3 (i.e., 7.52 eV) was carefully measured using energy loss spectra of O1s for the Al_2O_3 (See Figure 3.4(b)).[28] Using the valence band offset and band gap of the Si and Al_2O_3 in Eq. (2), the conduction band offset was finally determined to be 2.45 eV. It

should be noted that the measured Al_2O_3/Si NM conduction band offset is larger than those reported from other material systems such as AlN/GaN (i.e., 2.1 eV)[29], AlGaAs/GaAs (i.e., 0.4 eV),[9] and Si/SiGe (i.e., 0.17 eV)[8] which results in a large peak-to-valley current ratio (PVCR) and multiple NDR points from our Al_2O_3/Si NM based RTDs.

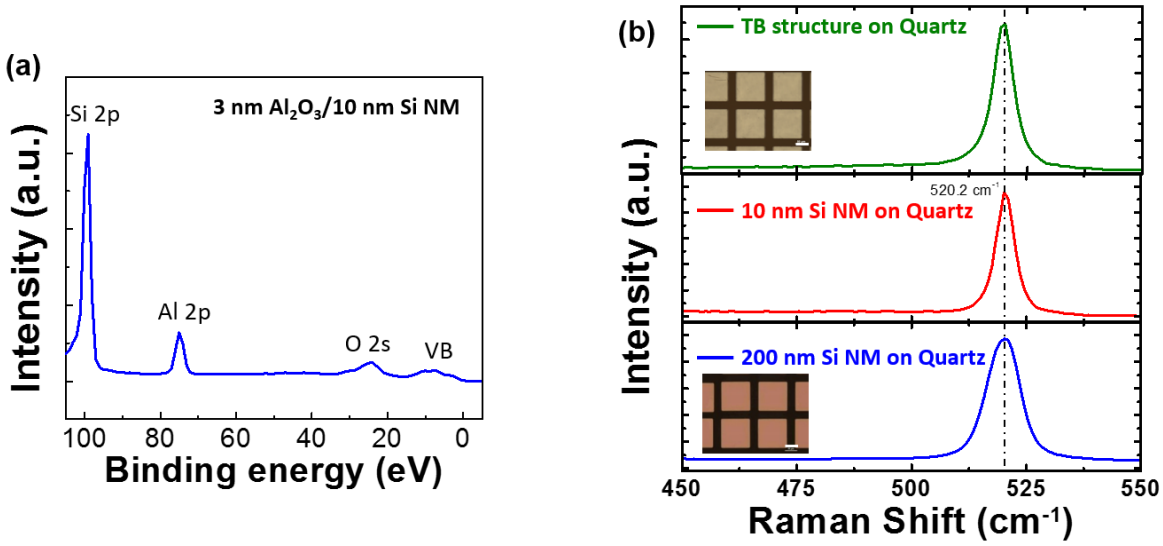

Figure 3.3. ***(a)*** *XPS spectrum measured from 3 nm Al_2O_3/10 nm Si NM.* ***(b)*** *Raman spectra measured from 200 nm Si NM, 10 nm Si NM, and 3 nm Al_2O_3 / 10 nm Si NM / 3 nm Al_2O_3 / 10 nm Si NM / 3 nm Al_2O_3 on Quartz, respectively. Inset shows the microscopic images of (top) 3 nm Al_2O_3 / 10 nm Si NM / 3 nm Al_2O_3 / 10 nm Si NM / 3 nm Al_2O_3 on Quartz substrate, and (bottom) 200 nm Si NM. The scale bar in the inset is 50 μm.*

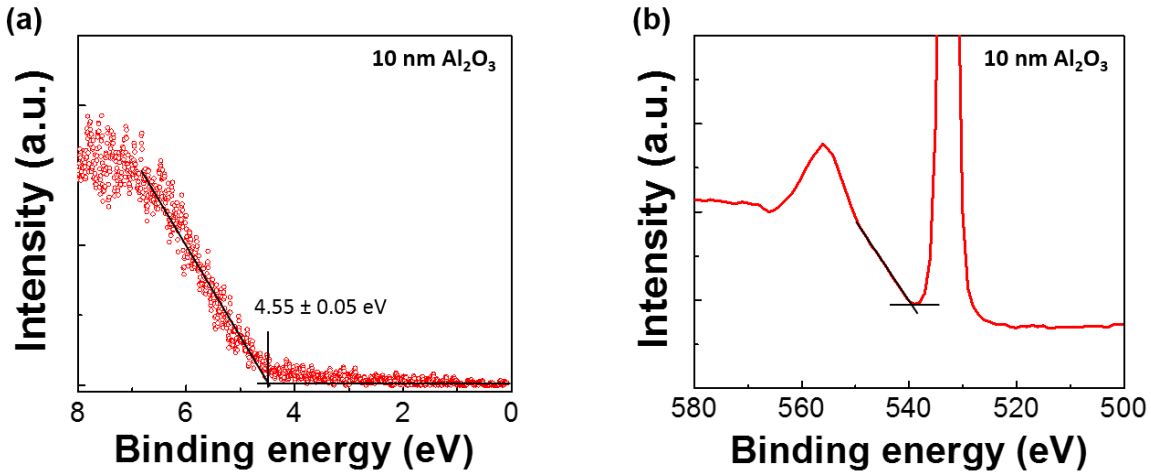

Figure 3.4. (a) *Valence band photoelectron spectrum measured from 10 nm thick Al_2O_3.* ***(b)*** *O1s energy loss spectra measured from the same sample.*

In conventional SiGe based RTDs, an increased conduction band offset can be achieved by applying compressive strain in $Si_{1-x}Ge_x$ barriers.[30] Although this approach effectively enhanced a NDR characteristic at RT, complex growth controls of each layer were required to obtain the desirable strain condition in the $Si_{1-x}Ge_x$ wells and Si barriers. We examined the possible existence of strain on the transferred Si NM that may be induced during the high temperature processes used for the thinning of Si NM. We also paid attention on the possible effects of NM bonding to the material properties of the Si NM and to the quality of the MBH. To trace a strain condition during thinning down and stacking processes, Raman spectroscopy was carefully performed on the Si NM after each thinning step. A 50× objective lens was used to focus a green laser (532 nm) onto the sample surface. Typical Raman spectra of the Si NM are shown in Figure 3.3(b). We measured a Si substrate as a reference and confirmed a strong Si-Si characteristic peak at 520.2 cm^{-1}.[31] A 200 nm thick Si NM, taken after the transfer on the quartz substrate, also showed a strong peak at 520.2 cm^{-1}. A 10 nm thick Si NM, which was transferred and thinned down on the quartz substrate still showed a clear Si characteristic peak at 520.2 cm^{-1} with a slightly weaker intensity. This

indicates that a strain-free thin Si NM was achieved using our thinning process. To evaluate the strain condition of the stacked layers used in the device, the TB structure was prepared on the quartz substrate. The sample was annealed under the same condition (i.e., 300℃ for 5 minutes) used in the device fabrication to mimic the thermal budget. A strong Si-Si characteristic peak was measured at 520.2 cm^{-1}. As a result, ultra-smooth thin Si NM was formed with no built-in strain. It should be noted that no strain was induced from the thinning/stacking of Si NMs or the annealing step for the Si NM bonding. Therefore, the stacking of multiple layers of Si NM and Al_2O_3 by NM transfer can easily realize a large conduction band offset without complicated and delicate strain engineering.

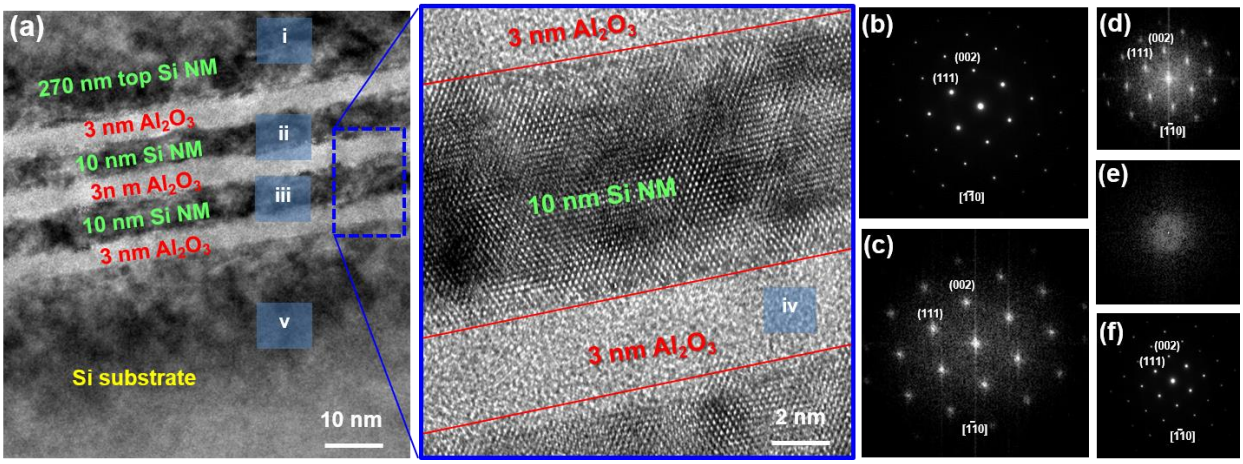

Figure 3.5. *HRTEM image of the triple barrier structure and electron diffraction pattern of each layer:* ***(a)*** *A cross-sectional TEM image taken from the TB structure; (i) top Si NM (ii) 2nd Si NM well layer (iii) 1st Si NM well layer (iv) Al_2O_3 barrier layer (v) Si substrate.* ***(b)-(f)*** *electron diffraction patterns of layer of i, ii, iii, iv, and v, respectively.*

Figure 3.5 shows the cross-sectional HRTEM images of the TB structure, clearly demonstrating two distinct layers of Si NMs interdigitated by three layers of Al_2O_3. Electron diffraction patterns (Figure 3.5(b) and (c)) taken from the top Si NM layer and Si substrate

indicated high crystalline quality for both subjects. HRTEM images and the corresponding Fast Fourier Transform (FFM) (Figure 3.5(d) and (e)) of two ultrathin Si NMs (~10 nm thick) confirmed their single crystallinity property and great crystallographic lattice alignment with both the Si substrate and top Si NM. It was observed that the Al_2O_3 tunneling layer remained amorphous (Figure 3.5(f)) and became slightly thicker, possibly due to the reflow of Al_2O_3 barrier layer to fill the atomic void between the Al_2O_3 layer and the bottom side of the transfer-printed Si NM during RTA annealing and thus consolidated transferred Si NMs. Such an atomically tight bonding could be ascribed to the NDR at RT.

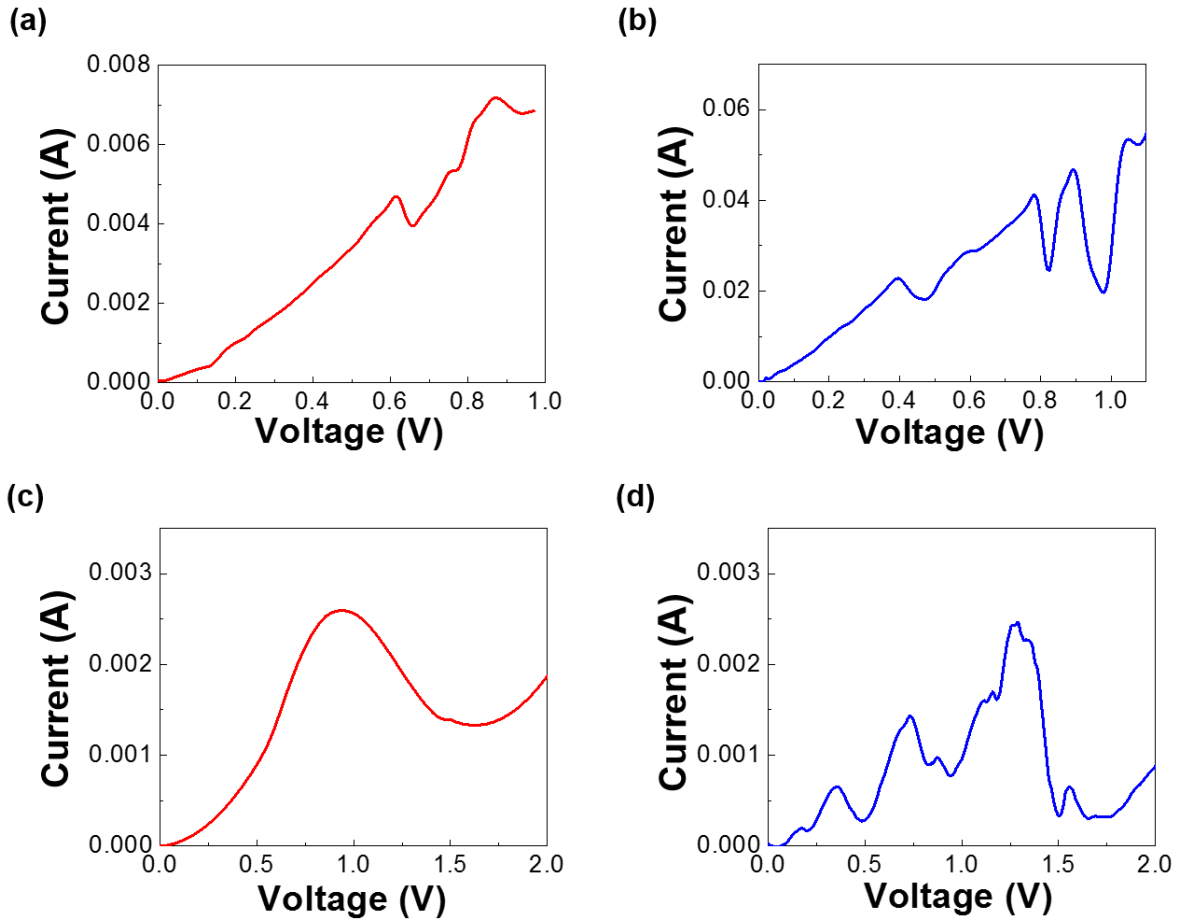

Figure 3.6*. Electrical properties of the double (i.e., Si NM/Al_2O_3/Si NM/Al_2O_3/ Si substrate) and triple barrier (i.e., Si NM/Al_2O_3/Si NM/Al_2O_3/Si NM/Al_2O_3/ Si substrate) RTDs: Current-voltage*

(I−V) characteristics measured from DB RTDs ***(a)*** *at RT and* ***(b)*** *at 77 K. (I−V) characteristics measured from TB RTDs* ***(c)*** *at RT and* ***(d)*** *at 77 K.*

Figure 3.6(a)-(d) show the typical current-voltage (*I-V*) characteristics of DB and TB RTDs measured at RT and 77 K, respectively. *I-V* curves were measured using an HP4155A semiconductor parameter analyzer under dark ambient to prevent any possible photocurrent. The entire stage and samples were continuously chilled with liquid nitrogen during the low temperature measurement. Clear NDR characteristics were observed from both devices at RT. Two NDR points from DB RTDs appeared at 0.635 V and 0.895 V with PVCRs of 1.19 and 1.06, respectively, as shown in Figure 3.6(a). Figure 3.6(c) shows a clear NDR observed from TB configuration at 1.1 V with a PVCR of 1.95, which was larger than that of the DB RTD. The second well of the TB structure could block electron tunneling at higher energy levels and, thus it resulted in a low valley current with a more distinct NDR. The peak and valley current of the first NDR point of the DB RTD was measured to be 4.69 mA and 3.95 mA, respectively. The second NDR point was measured with a peak current of 7.16 mA and valley current of 6.78 mA. The peak and valley current of 2.59 mA and 1.33 mA, respectively, were measured from TB RTD. As the bias increased, both peak and valley currents increased with the valley current increasing faster than the peak current, resulting in a smaller second PVCR.

Figure 3.6(b) shows the low temperature *I-V* characteristic of the DB RTD measured at 77 K. Four NDR points were clearly observed at 0.415 V, 0.805 V, 0.915 V, and 1.06 V with PVCRs of 1.25, 1.67, 2.38, and 1.02, respectively. The current measured at 77 K increased approximately one order of magnitude compared to that measured at RT. Such a temperature-dependent current behavior could be attributed to temperature-associated semiconductor physics properties such as carrier distribution, the position of the Fermi level, and electron scattering.[32] The supply function

of an incoming electron becomes broadened at elevated temperatures and results in the non-resonant component of the tunneling current. Moreover, scattering at the interface further decreases the resonant transmission probability through the resonant tunneling structure at elevated temperatures.[23] Figure 3.6(d) shows the low temperature *I-V* characteristic of the TB RTD. A similar trend (i.e., increased number of NDR points at 77 K) was observed. Five NDR points were measured at 0.395 V, 0.77 V, 0.9 V, 1.42 V, and 1.59 V with PVCRs with 2.38, 1.6, 1.26, 7.48, and 2.14, respectively. Multiple points of NDR observed from DB and TB configurations at 77 K resulted from multiple resonant energy states formed by a large conduction band offset (i.e., 2.45 eV).

3.4 Conclusion

In conclusion, we have demonstrated a novel method of creating single crystalline Si NM-amorphous oxide based MBHs on Si substrates by using Si NM stacking processes, which eliminates epitaxial growth and lattice match requirements. Such stacked MBH provides the largest conduction band offset that allows deep quantum well confinement. The demonstrations of the delicately structured RTDs with large PVCR values and multiple NDR points prove the viability, materials versatility, and processing feasibility of the new method of forming MBHs. Considering that RTDs are building blocks of quantum cascade lasers (QCL), the work shed light on Si-based QCL, which could be a subject of future study.

3.5 Reference

1 R. Tsu and L. Esaki, “Tunneling in a finite superlattice”, *Appl. Phys. Lett.* **22**, 562 (1973)

2 L. L. Chang, L. Esaki, and R. Tsu, “Resonant tunneling in semiconductor double barriers”, *Appl. Phys. Lett.* **24**, 593 (1974)

3 T. C. L. G. Sollner, W. D. Goodhue, P. E. Tannenwald, C. D. Parker, and D. D. Peck, “Resonant tunneling through quantum wells at frequencies up to 2.5 THz”, *Appl. Phys. Lett.* **45**, 588 (1983)

4 S. Ray, P. Ruden, V. Sokolov, R. Kolbas, T. Boonstra, and J. Williams, “Resonant tunneling transport at 300 K in GaAs-AlGaAs quantum wells grown by metalorganic chemical vapor deposition”, *Appl. Phys. Lett.* **48**, 1666 (1986)

5 T. J. Shewchuk, P. C. Chapin, P. D. Coleman, W. Kopp, R. Fisher, and H. Morkoç, “Resonant tunneling oscillations in a GaAs-$Al_xGa_{1-x}As$ heterostructure at room temperature”, *Appl. Phys. Lett.* **46**, 508 (1985)

6 M. Ohring, *The Materials Science of Thin Films*, Academic, London (1991)

7 K. Ismail, B. S. Meyerson, and P. J. Wang, “Electron resonant tunneling in Si/SiGe double barrier diodes”, *Appl. Phys. Lett.* **59**, 973 (1991)

8 H. C. Liu, D. Landheer, M. Buchanan, and D. C. Houghton, “Resonant tunneling in $Si/Si_{1-x}Ge_x$ double-barrier structures”, *Appl. Phys. Lett.* **52**, 1809 (1988)

9 S. Ray, P. Ruden, V. Sokolov, R. Kolbas, T. Boonstra, and J. Williams, “Resonant tunneling transport at 300 K in gallium arsenide-aluminum gallium arsenide quantum wells grown by metalorganic chemical vapor deposition”, *Appl. Phys. Lett.* **48**, 1666 (1986).

10 T. Nakagawa, H. Imamoto, T. Kojima, and K. Ohta, "Observation of resonant tunneling in AlGaAs/GaAs triple barrier diodes", *Appl. Phys. Lett.* **49**, 73 (1986)

11 H. Ikeda, M. Iwasaki, Y. Ishikawa, and M. Tabe, "Resonant tunneling characteristics in SiO_2/Si double-barrier structures in a wide range of applied voltage", *Appl. Phys. Lett.* **83**, 1456 (2003)

12 D. J. Lockwood, Z. H. Lu, and J.-M. Baribeau, "Quantum Confined Luminescence in Si/SiO2 Superlattices", *Phys. Rev. Lett.* **76**, 539 (1996)

13 R. Lake, B. Brar, G. G. Wilk, A. Seabaugh, and G. Klimeck, "Resonant Tunneling in Disordered Materials such as SiO_2/Si/SiO_2", *IEEE International Symposium on Compound Semiconductors*, pp. 617-620, San Diego, USA, September (1997)

14 M. Shahjahan, Y. Koji, K. Sawada, and M. Ishida, "Fabrication of Resonance Tunnel Diode by γ-Al_2O_3/Si Multiple Heterostructures", *Jpn. J. Appl. Phys.*, Vol. 41, pp. 2602-2605 (2002)

15 M. Watanabe, Y. Iketani, and M. Asada, "Epitaxial Growth and Electrical Characteristics of CaF_2/Si/CaF_2 Resonant Tunneling Diode Structures Grown on Si(111) 1°-off Substrate", *Jpn. J. Appl. Phys.*, Vol. 39, pp. L964-L967 (2000)

16 Y. Ishikawa, T. Ishihara, M. Iwasaki, and M. Tabe, "Negative differential conductance due to resonant tunnelling through SiO_2/single-crystalline-Si double barrier structure", *IET Electronics Letters*, Vol. 37, No. 19, pp. 1200-1201 (2001)

17 T. H. Lee, H. C. Frolesca, S. J. Kang, J. J. Shim, K. H. Song, H. B. Kang, B. Y. Lee, R. M. Wallace, B. E. Gnade, and M. J. Kim, "Fabrication Process for Double Barrier Si-Based Quantum Well Resonant Tunneling Diodes (RTD) by UHV Wafer Bonding", *ECS Transactions*, 16(8), pp. 525-530 (2008)

18 H. Yang, D. Zhao, S. Chuwongin, J.-H. Seo, W. Yang, Y. Shuai, J. Berggren, M. Hammar, Z. Ma, and W. Zhou, "Transfer-printed stacked nanomembrane lasers on silicon", *Nature Photonics* Vol. 6, pp. 615-620 (2012)

19 M. Cho, J.-H. Seo, J. Lee, D. Zhao, H. Mi, X. Yin, M. Kim, X. Wang, W. Zhou, and Z. Ma, "Ultra-thin distributed Bragg reflectors via stacked single-crystal silicon nanomembranes", *Appl. Phys. Lett.* **106**, 181107 (2015)

20 J. A. Rogers, M. G. Lagally, and R. G. Nuzzo, "Synthesis, assembly and applications of semiconductor nanomembranes", *Nature* **477**, 45-53 (2011).

21 B. Hoex, S. B. S. Heil, E. Langereis, M. C. M. van de Sanden, and W. M. M. Kessels, "*In situ* reaction mechanism studies of plasma-assisted atomic layer deposition of Al_2O_3", *Appl. Phys. Lett.* **89**, 042112 (2006)

22. M. A. Meitl, Z.-T. Zhu, V. Kumar, K. J. Lee, X. Feng,Y.Y. Huang, I. Adesida, R. G. Nuzzo, J. A. Rogers, "Transfer printing by kinetic control of adhesion to an elastomeric stamp" *Nature* **5**, 33-38 (2006).

23 M. R. Brown, P. Rees, R. J. Cobley, K. S. Teng, S. Wilks, and A. Hughes, "The effect of interface roughness on multilayer heterostructures", *J. Appl. Phys.*, **102**, 113711 (2007)

24 M. Martin and G. Cunge, "Surface roughness generated by plasma etching processes of silicon", *J. Vac. Sci. Technol. B* **26**, 1281 (2008)

25 L. M. Ephrath and R. S. Bennett, "RIE Contamination of Etched Silicon Surfaces", *J. Electrochem. Soc.* Vol. 129, No. 8 pp. 1822-1826 (1982)

26 S. A. Chambers, Y. Liang, Z. Yu, R. Droopad, J. Ramdani, and K. Eisenbeiser, "Band discontinuities at epitaxial heterojunctions", *Appl. Phys. Lett.* **77**, 1662 (2000)

27 L. Kornblum, M. D. Morales-Acosta, E. N. Jin, C. H. Ahn, and F. J. Walker, "Transport at the Epitaxial Interface between Germanium and Functional Oxides", *Adv. Mater. Interfaces,* Vol. 2, Issue 18 (2015)

28 S. Miyazaki, "Characterization of high-k gate dielectric/silicon interfaces", *Appl. Surf. Sci.,* 190, pp.66-74 (2002)

29 C. Bayram, Z. Vashaei, and M. Razeghi, "AlN/GaN double-barrier resonant tunneling diodes grown by metal-organic chemical vapor deposition", *Appl. Phys. Lett.*, **96**, 042103 (2010)

30 P. See, D. J. Paul, B. Hollander, S. Mantl, I. V. Zozoulenko, and K.-F. Berggren, "High performance Si/Si/sub 1-x/Ge_xresonant tunneling diodes", *IEEE Electron Device Lett.*, Vol. 22, No. 4 (2001)

31 J. C. Tsang, P. M. Mooney, F. Dacol, and J. O. Chu, "Measurements of alloy composition and strain in thin $Ge_x Si_{1-x}$ layers", *J. Appl. Phys.*, **75**, 8098 (1994)

32 J. Chen, J. G. Chen, C. H. Yang, and R. A. Wilson, "The *I-V* characteristics of double-barrier resonant tunneling diodes: Observation and calculation on their temperature dependence and asymmetry", *J. Appl. Phys.*, **70**, 3131 (1991)

Chapter 4. Engineering light enhancement in Ge nanomembrane and its optoelectronic application

4.1 Introduction

Germanium (Ge) has been a key semiconductor material in photonic and optoelectronic applications in the NIR wavelength range due to its superior light absorption property.[1,2] Especially, Ge based photodetectors designed for the wavelength of 1.55 μm are critically important because optical fiber for long-haul communication has the lowest loss around this wavelength.[3] Considering the material compatibility of Ge with Si, extending the Ge light absorption capability into longer wavelengths beyond 1.55 μm is significant for silicon (Si)-based on-chip communication because Si waveguide has a lower propagation loss in longer (than 1.55 μm) wavelengths.[4] However, Ge photodetectors typically suffer from low responsivity at wavelengths longer than 1.55 μm due to the abrupt drop in its absorption coefficient that begins at ~1.5 μm.[5] Therefore, strategies to improve the Ge light absorption beyond 1.55 μm have been sought and intensive research has been carried out to enhance the absorption of Ge in the NIR wavelength range.[6,7]

In recent years, Ge nanomembrane (Ge NM), which has a thickness that ranges from several tens of nanometers to hundreds of nanometers, exhibited its importance in optoelectronic applications. Ge based infrared optical gain media and flexible Ge photodetectors have been demonstrated.[8,9,10] The Ge on insulator (GeOI) wafers, which are the source materials of Ge NMs, have been created either by using epitaxy growth (e.g., on top of a temporary/sacrificial GaAs substrate) or a Smart-Cut® process (the most widely used).[11,12] In the Smart-Cut® process,

hydrogen (H) ion implantation is used to split the transferrable thin Ge layers from the bulk Ge wafer.[13] Annealing the H implanted Ge wafer induces the exfoliation of the Ge layer from bulk Ge wafer.[14] The damaged Ge layer by implanted H ions can be mostly removed by the subsequent chemical mechanical planarization (CMP) process. However, it is reported that high concentrations of vacancies in the order of 10^{21} /cm^3 are created in Ge during ion implantation.[15] Residual H ions still exist inside the Ge layer, with a concentration range of $10^{19} \sim 10^{20}$ /cm^3.[15] Although a thicker (like bulk) Ge layer has the advantage of better light absorption, a thinner Ge layer (e.g., Ge NM) for its unique mechanical and other related properties has more versatile use than the thicker ones. Regardless of the thickness, the light absorption coefficient of Ge (i.e., both bulk Ge and Ge NM) decreases rapidly at wavelengths longer than 1.5 μm.[5] Therefore, it is desirable to enhance the light absorption coefficient of Ge so that the total light absorption can be greatly enhanced in Ge-based optical sensor applications for both long haul and on-chip optical communications.

In this paper, we report a thorough analysis of light absorption of the Ge NM associated with H ion implantation. The optical properties of H-implanted Ge layer in GeOI wafers were characterized and it was found that the refractive index and the extinction coefficient can be manipulated by H implantation. In general, light absorption of semiconductor material increases with higher doping concentration and structural defects.[16,17] Previously, it was reported that the optical properties of GaAs were modified by H implantation.[18] However, such experiment of using H implants to modify the optical properties of Ge has never been reported. Here we report the demonstration of the enhancement of light absorption of H-implanted Ge NM. The enhanced light absorption of H implanted Ge was further confirmed by investigating the responsivity of metal-semiconductor-metal (MSM) photodetectors that are fabricated using the H-implanted Ge NM.

4.2 Experiment

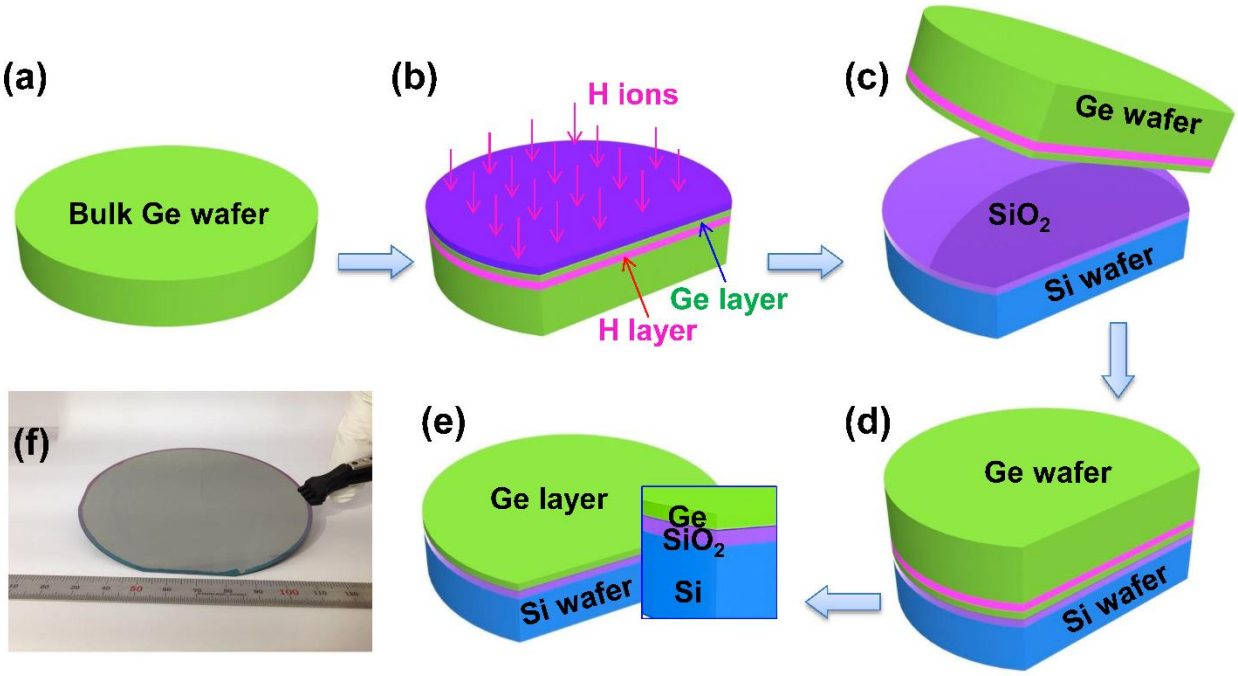

Figure 4.1. *A schematic process flow of the fabrication of GeOI wafer:* ***(a)*** *Cleaning a bulk Ge wafer.* ***(b)*** *Depositing a 100 nm thick PECVD SiO_2 layer on top of the Ge wafer followed by hydrogen implantation.* ***(c)*** *Wafer bonding to thermally oxidized Si handling wafer.* ***(d)*** *Annealing the bonded wafers for splitting Ge layers by hydrogen exfoliation.* ***(e)*** *Polishing a transferred Ge layer to the desired thickness to achieve a smooth surface roughness.* ***(f)*** *An optical image of the fabricated GeOI wafer.*

Figure 4.1 shows the fabrication process flow of the GeOI wafers. The process began with an unintentionally doped 4-inch intrinsic bulk Ge wafer with a resistivity larger than 40 Ω-cm (Figure 4.1(a)). A 100 nm thick plasma enhanced chemical vapor deposition (PECVD) SiO_2 layer was deposited on the Ge wafers as a screen oxide in order to obtain a uniform ion implantation profile.[19] The oxide-capped Ge wafers were implanted by H+ ions with a dose of 1×10^{17} cm^{-2} and an energy of 100 keV (Figure 4.1(b)). The peak position of the hydrogen implantation profile was

carefully designed to be placed at 700 nm from the Ge surface in order to acquire a 400 nm thick Ge layer after the splitting process. A 200 nm thick SiO_2 was grown on a Si handling substrate as the buried oxide (BOX) layer for the final structure of the GeOI. Prior to the wafer bonding between the H implanted Ge wafers and the oxidized Si substrate, the PECVD SiO_2 was removed from the Ge substrate using concentrated hydrofluoric acid (HF, 49%) and an oxygen plasma activation process on a SiO_2/Si substrate was carried out to enhance the bonding strength. The wafer bonding process was performed using a direct wafer bonder (EV 801) under a vacuum of 7×10^{-5} mbar (Figure 4.1(c)). After finishing physical contact between the H implanted Ge wafer and the SiO_2/Si wafer in the wafer bonder, a careful temperature control during the annealing step with a ramp up/down of 1℃/min was applied to avoid fracture of bonded wafers due to their different coefficients of thermal expansion.[20] In addition to the annealing process in the wafer bonder, a two-step, low temperature annealing at 200℃ and 250℃ were carried out in a nitrogen-filled oven to improve the nucleation of hydrogen platelets to achieve a complete separation of the Ge layer from the Ge bulk substrate (Figure 4.1(d)-(e)). A ~700 nm thick Ge layer with the rough surface facing up was successfully transferred onto the SiO_2/Si handling wafer without any visible voids. The rough Ge surface, which has a root mean square (RMS) value (R_q) of 22 nm, was polished down to 0.5 nm, giving a final Ge thickness of about 400 nm (Figure 4.1(e)).

To investigate the effect of thermal annealing on the electrical and optical properties of Ge layer, the finished GeOI wafer was annealed using rapid thermal annealing (RTA) at 600℃ for 3 minutes in nitrogen ambient. Transfer length measurements (TLM) were carried out on as-fabricated (non-annealed: NA) and annealed (A) GeOI wafers with three different thicknesses of Ge layers (i.e., 400, 175, and 50 nm) to quantify the free-carrier concentrations inside the Ge layer.

To characterize the optical properties of the Ge layer of the GeOI wafer, the Ge layer was released from the GeOI wafer and transferred onto a transparent plastic substrate. The detailed process can be found elsewhere.[21] In short, the top Ge layer was patterned and undercut in HF (49%) solution to remove the BOX layer. The released top Ge layer, now called the Ge NM, was flip-transferred onto a 1 μm thick adhesive layer (Microchem, SU-8 2002) coated on 180 μm thick polyethylene terephthalate (PET) film. Transferred Ge NMs (size: 5 × 5 mm^2) were completely glued to the PET films by a UV curing process. The Ge NM reflection and transmission spectra were measured at room temperature using a custom-built reflection and transmission system. Both the reflection and the transmission were measured from surface normal incidence using a white light source which has a spectral range of 1000 ~ 1600 nm and the spectra were collected using two fiber coupling adapters that were connected to an optical spectrum analyzer (Yokogawa, AQ6370B), simultaneously.

Finally, MSM photodiodes were fabricated on non-annealed and annealed GeOI wafers to illustrate the improved photo responsivity of the H incorporated Ge layer. Interdigitated metal electrodes (Ti/Au = 50/450 nm) with a 2 μm width and a 6 μm distance between the electrodes were e-beam evaporated on the 40 × 70 μm^2 patterned Ge layer, followed by the deposition of a 250 nm thick PECVD SiO_2 layer and the opening of the contact windows. I-V characteristics of the fabricated devices were measured using a semiconductor parameter analyzer (HP4155B) under dark and illuminated conditions. Infrared light at wavelengths of 1.5, 1.55, 1.6, and 1.64 μm was focused on the device via a lensed fiber with incident powers of 70, 125, 180, and 200 μW, respectively.

4.3 Experimental Results and Discussion

Figure 4.1(f) shows an optical image of a finished 4-inch GeOI wafer and its corresponding cross-sectional scanning electron microscopy (SEM) image is shown in Figure 4.2(a), for which the buried interfaces after annealing at 250 ˚C for 1 hour and the subsequent CMP process were applied. The thicknesses of the Ge layer and the BOX layer were measured to be 400 and 200 nm, respectively. These values corresponded well with our target layer thicknesses.

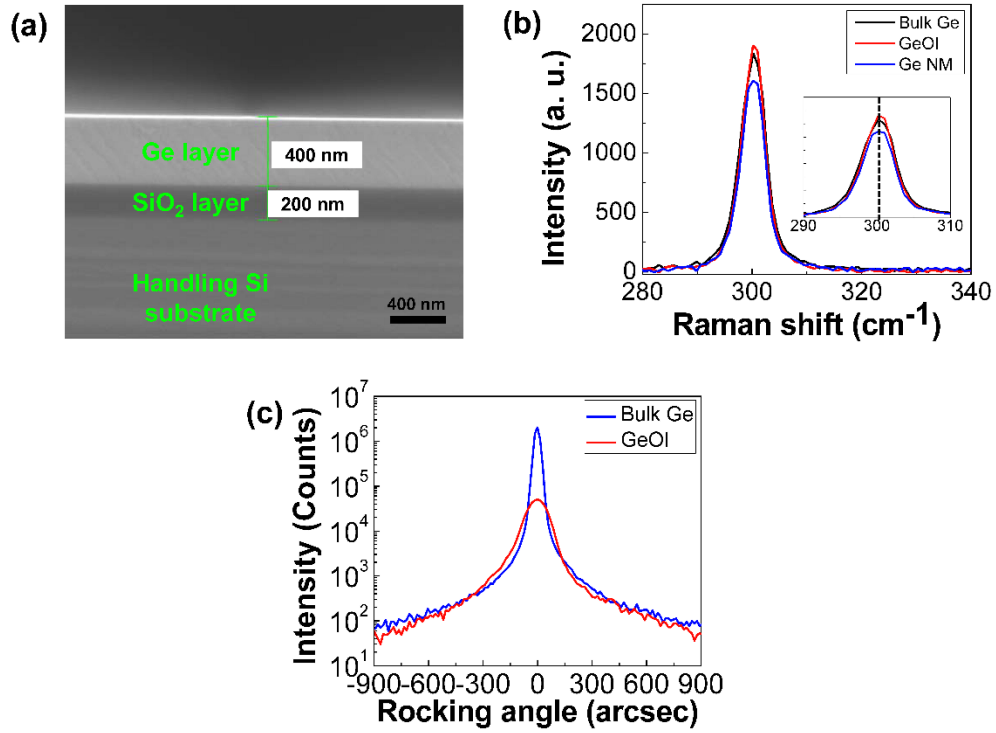

Figure 4.2. ***(a)*** *A cross-sectional SEM image of the GeOI wafer.* ***(b)*** *Measured Raman spectra from bulk Ge wafer, GeOI wafer, and Ge NM on PET substrate, respectively.* ***(c)*** *HR-XRD rocking curves of the bulk Ge and GeOI.*

It is important to note the crystallinity and the residual strain of the Ge layer in the fabricated GeOI wafer, since the process for the GeOI wafer fabrication involves several steps of thermal processes with high pressure. Horiba LabRAM ARAMIS Raman spectroscopy with a

green laser (532 nm) was used to investigate the material properties from the top surface of the Ge layer. Figure 4.2(b) shows a comparison of the Raman spectrum taken from a bulk Ge wafer, the Ge layer in our fabricated GeOI wafer, and the as-transferred Ge NM on PET substrate, respectively. The bulk Ge wafer was used as the reference, which has a Ge-Ge characteristic peak at 300.29 cm^{-1}.[22] The same 300.29 cm^{-1} Ge-Ge characteristic peaks from other two cases (i.e., the Ge layer in GeOI wafer and as-transferred Ge NM on PET substrate) confirmed that no strain was introduced in the Ge layer of the GeOI wafer or in the released and transferred Ge NM. We investigated full width at half maximum (FWHM) of the bulk Ge and GeOI using high resolution X-ray diffraction (HR-XRD, PANalytical X'Pert PRO XRD). Rocking curves of both samples were scanned around the (004) reflection as shown in Figure 4.2(c). The FWHM of the bulk Ge was measured to be 43 arcsec, while it increased to 124 arcsec measured from the GeOI. The increased FWHM was probably caused by the structural defects associated with H ion implantation.

It is known that ion implantation can be used to manipulate optical and electrical properties of semiconductors.[23,24] Among various ions used for implantation, H+ ions have been used for various applications, such as optical waveguide, electrical isolation, and semiconductor laser fabrication.[25,26,27] H implantation introduces high concentrations of vacancies in Ge. In addition, residual H+ ions remain inside of the Ge layer of the GeOI wafer, as a result of H implantation when splitting the Ge layer from the bulk Ge wafer. The residual H+ ions combine with these Ge vacancies to form V_2H with an acceptor energy level of 0.08 eV above the valence band of Ge.[28] It is reported that approximately 0.3% of the residual H+ ions are electrically active and can act as acceptors.[15] A comparison of the free-carrier (hole) concentration, extracted from the TLM measurement results, is shown in Figure 4.4(a). The TLM patterns with a pad spacing from 10 to 50 μm with a step of 10 μm were fabricated on GeOI wafers with various thicknesses of the Ge

layer (i.e., 400, 175, 50 nm). Figure 4.3 shows the contact resistance (R_c) and sheet resistance (R_{sh}) measured from the TLM. They can be calculated from total resistance (R_T) using the following equation.

$$R_T = \frac{R_{sh}}{W} \times L + 2R_c = slope \times L + 2R_c \qquad (1)$$

where R_T is total resistance, R_{sh} the sheet resistance, R_c the contact resistance, and W and L the width and length of the TLM pattern. Based on the measured R_{sh}, bulk resistivity can be calculated by multiplying film thickness by the sheet resistance. Based on Eq. 1, the resistivities of non-annealed and annealed GeOI wafers were calculated to be 1.1 and 27.6 Ω·cm, respectively. They correspond to the concentrations of 3.1×10^{15} and 1.14×10^{14} cm^{-3}, respectively. The concentration values of the GeOI wafers with other thicknesses presented in Figure 4.4(a) were obtained using the same method.

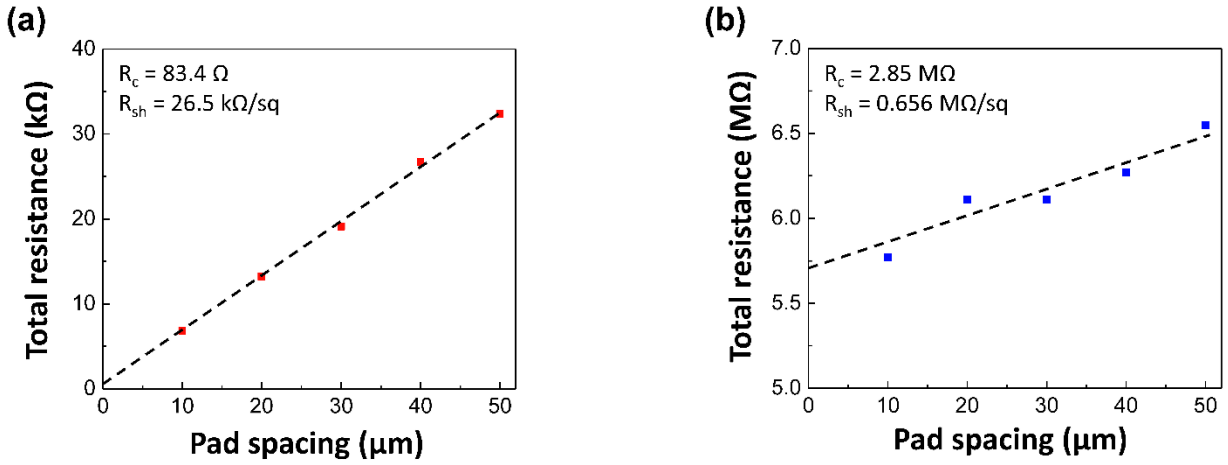

Figure 4.3. *Contact resistance (R_c) and sheet resistance (R_{sh}) extracted from TLM measurement:* ***(a)*** *TLM measured on non-annealed GeOI wafer.* ***(b)*** *TLM measured on annealed GeOI by RTA at 600℃ for 3 minutes.*

The free-carrier concentration of the Ge layer of the non-annealed (NA) GeOI wafer showed the highest value of 3×10^{15} cm^{-3} at the top surface of the Ge layer of the GeOI and is reduced to 5×10^{13} and 4×10^{13} cm^{-3} at the depth of 225 nm and 350 nm, respectively. In contrast, the free-carrier concentration in the Ge layer of the annealed GeOI wafer (1×10^{14} cm^{-3}) is lower by approximately an order of magnitude near the Ge top surface, although the free-carrier concentration eventually reached the similar values at the deeper regions. It should be noted that the measured free-carrier concentrations in the Ge layers of the GeOI wafers were greater than that of the bulk Ge wafer. The extra concentration of free carriers is ascribed to the electrically active acceptors that resulted from the residual H+. The higher free-carrier concentration near the top Ge surface (i.e., the deep regions of H implanted Ge wafer before splitting) of the GeOI wafer was observed, suggesting that the H distribution in the Ge layer is similar to the projected range (R_p) of the implanted H ions (See Figure 4.4 for SIMS profile of the residual H in the non-annealed Ge NM). A reduction of the free-carrier concentration can be largely attributed to recovered defects due to the thermal annealing.

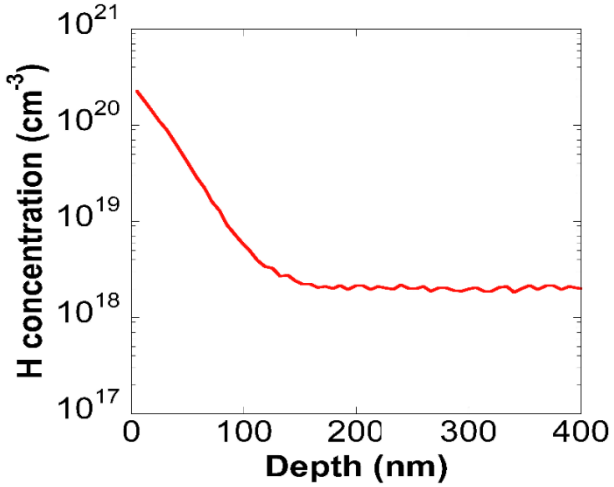

Figure 4.4. *SIMS profile of residual H+ ions in non-annealed Ge NM.*

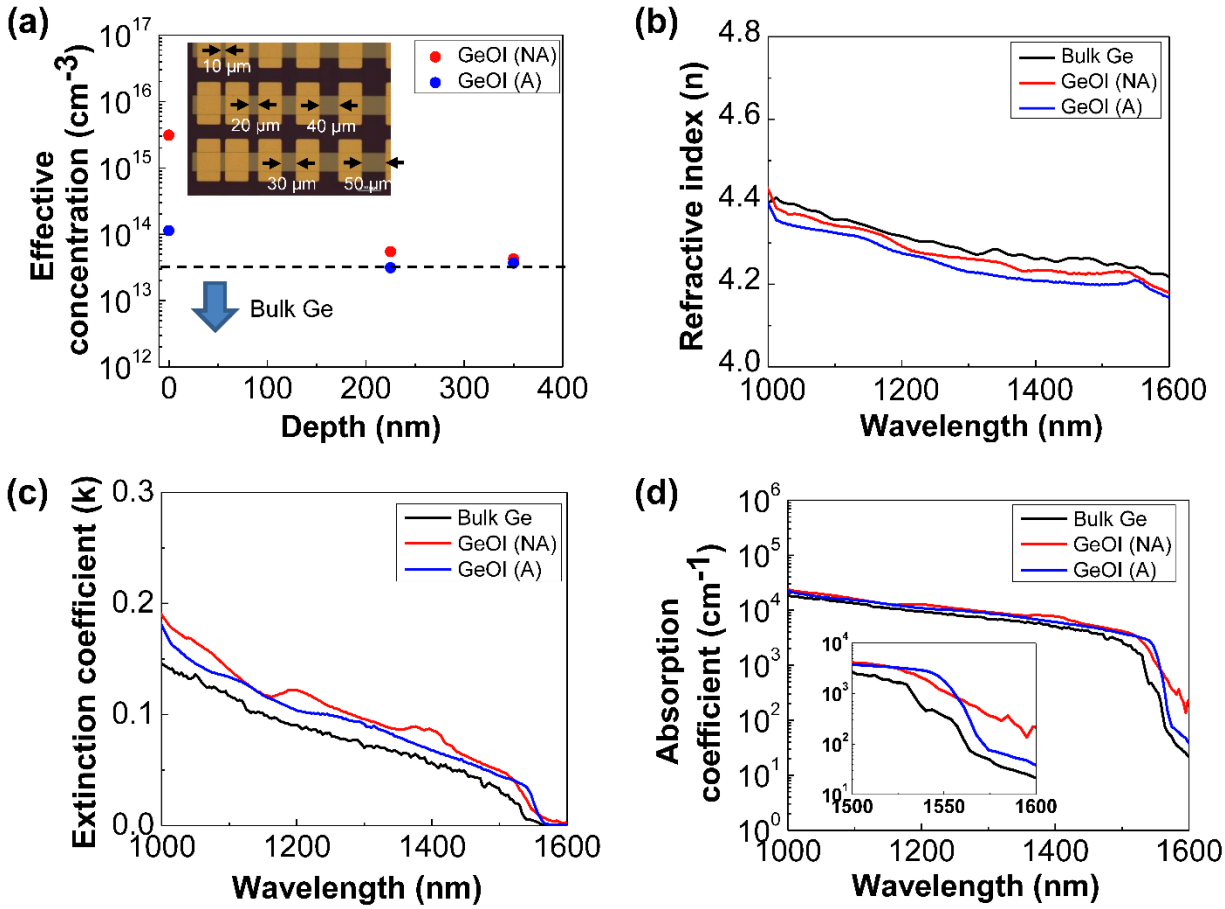

Figure 4.5. (a) *Measured free-carrier concentrations of Ge layers of non-annealed (NA) and annealed (A) GeOI wafers at 600℃ for 3 minutes. Inset shows a microscopic image of TLM patterns with various distances (i.e., 10, 20, 30, 40, and 50 μm) on Ge. Free-carrier concentration of bulk Ge wafer was presented for comparison.* ***(b, c)*** *Measured refractive indices and extinction coefficients of bulk Ge wafer and Ge layer of GeOI wafer in the case of NA and A at a wavelength range of 1000 ~ 1600 nm.* ***(d)*** *Absorption coefficient (α) of bulk Ge wafer and Ge layer of GeOI wafer calculated from the measured extinction coefficient (k) via $\alpha=4\pi k/\lambda$. The inset shows magnified absorption coefficient spectra in a wavelength of 1500 ~ 1600 nm.*

In order to evaluate the changes of optical properties of H-implanted Ge layer of the GeOI wafer, refractive indices and extinction coefficients of bulk Ge wafer, non-annealed, and annealed

GeOI wafers were carefully investigated using an ellipsometer (J. A. Woollam M-2000 DI) at a wavelength range of 1000 ~ 1600 nm. Figure 4.5(b) and (c) show the refractive indices and extinction coefficients taken from the bulk Ge wafer, non-annealed, and annealed GeOI wafers, respectively. The refractive index and extinction coefficient of the Ge film of the GeOI wafers were fitted by considering the measured refractive index and extinction coefficient of the BOX layer in a fitting model. The measured refractive index of the bulk Ge wafer agreed well with the values reported elsewhere.[29] The Ge layer of the non-annealed GeOI wafer exhibited a slightly decreased refractive index with a Δn of 0.024, and that of the annealed GeOI wafer further decreased with a Δn of 0.046, compared to that of the bulk Ge wafer. In contrast, the extinction coefficient of the non-annealed GeOI wafer increased, with a Δk of 0.027 compared to that of the bulk Ge wafer over the measured wavelength range. The extinction coefficient of the annealed GeOI wafer slightly decreased, with a Δk of 0.008 compared to that of the non-annealed GeOI wafer. The trend in our experiment (i.e., decreased refractive index and increased extinction coefficient) was ascribed to the defects introduced by H+ implantation. It should be noted that the effect of free-carrier concentration increase on the optical constants is negligibly small.[30] The absorption coefficient (α) of the Ge layer was calculated using the equation:

$$\alpha = (4 \times \pi \times k)/\lambda \qquad (2)$$

where α is the absorption coefficient, k the extinction coefficient, and λ the wavelength. As shown in Figure 4.5(d), the absorption coefficient of the GeOI wafer increased compared to that of the bulk Ge wafer.[9] The non-annealed GeOI wafer showed a further enhanced absorption coefficient. It is noted that the absorption enhancement is more significant at longer wavelengths than the shorter ones. The absorption coefficients at 1600 nm increased from 22 cm^{-1} for the bulk Ge wafer to 40 and 224 cm^{-1} for the annealed and non-annealed GeOI wafers, respectively. It should be

noted that our improvement in the absorption coefficient is not related to the tensile strain effect, as we confirmed it by Raman spectroscopy. Therefore, the absorption coefficient could be in fact further improved with the application of tensile strain.[31]

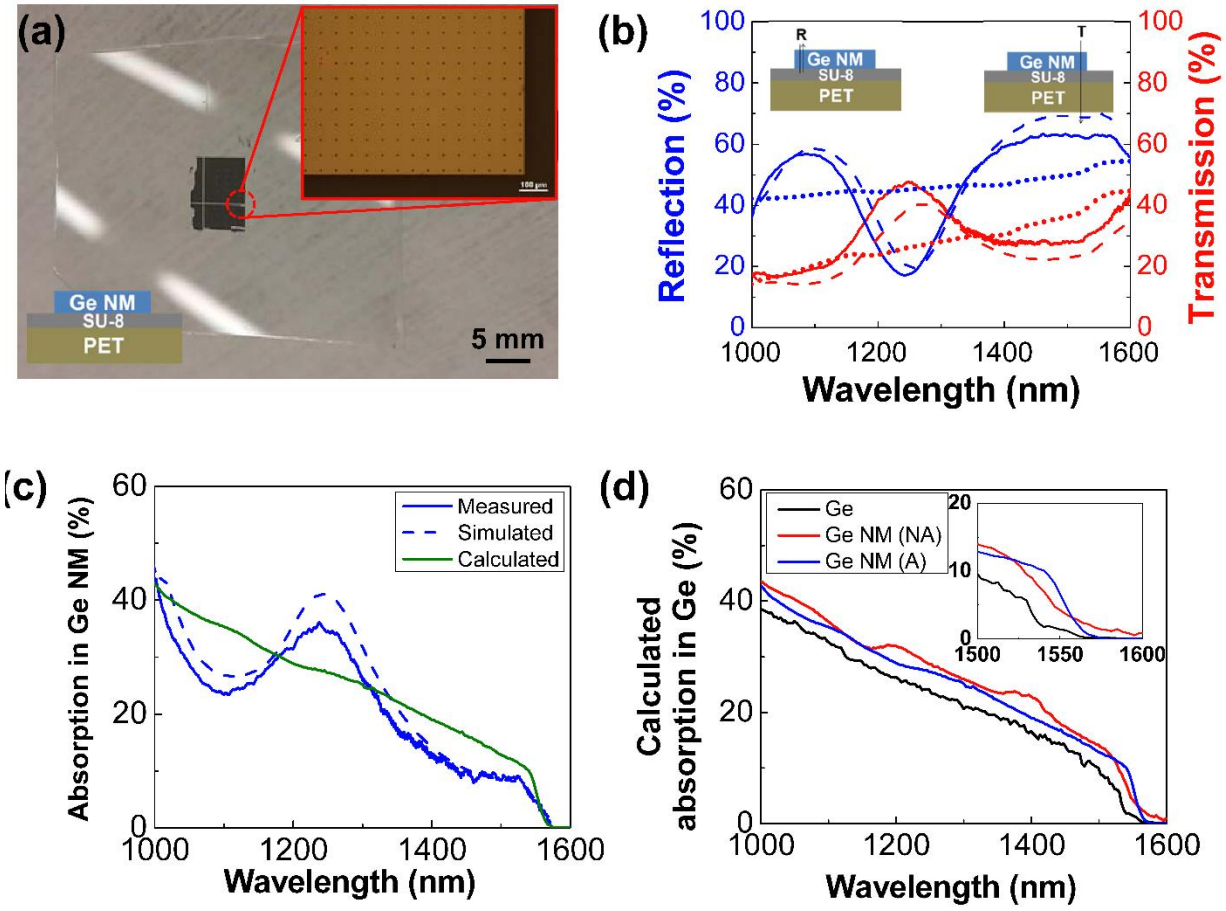

Figure 4.6. (a) *A microscopic image of the transferred Ge NM (size: 5 × 5 mm^2) on PET substrate. A bottom left inset shows a vertical layer structure of the sample and the top right inset shows the magnified image of the Ge NM.* ***(b)*** *Reflection and transmission spectra at a wavelength range of 1000 ~ 1600 nm. Note that the measured (solid line) and simulated (dashed line) spectra were obtained from Ge NM/SU-8/PET structure and calculated (dotted line) spectra came from the Ge NM.* ***(c)*** *Measured, simulated, and calculated absorption spectra of the Ge NM.* ***(d)*** *Comparison of the calculated absorption spectra from the Ge (not implanted) and Ge layer of GeOI wafer.*

Note that the same thickness of 400 nm was used. Inset shows magnified absorption spectra in a wavelength of 1500 ~ 1600 nm.

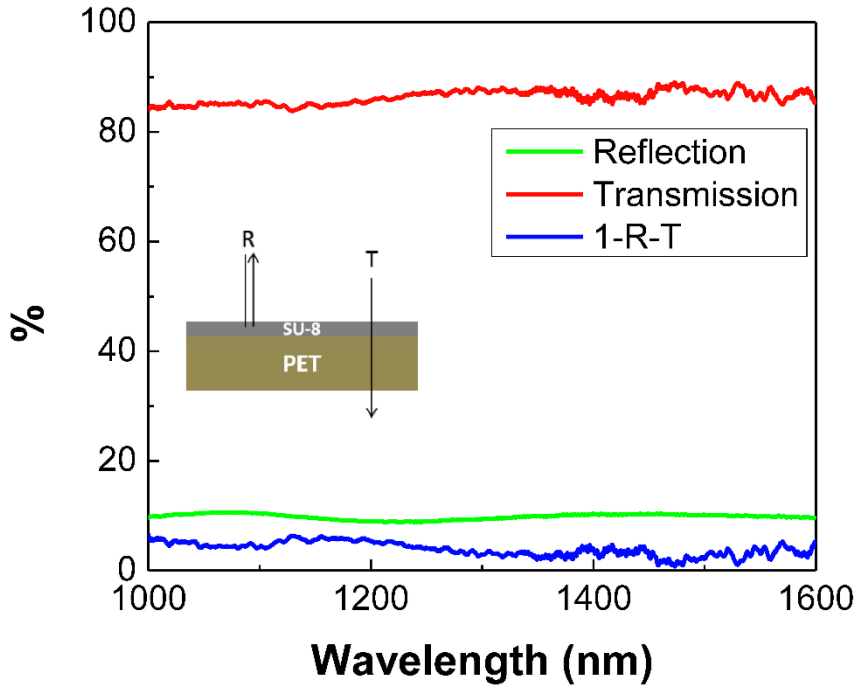

Figure 4.7. *Measured reflection (R), transmission (T), and 1-R-T of SU-8/PET stack.*

To further verify the light absorption of the Ge NM, we performed reflection and transmission measurements on SU-8/PET and Ge NM/SU-8/PET stacks. The Ge NM (released) from the annealed GeOI wafer was used in this experiment. Figure 4.6(a) shows the microscopic image of the Ge NM/SU-8/PET stack. The size of the transferred Ge NM (i.e., 5×5 mm^2) was made to be larger than spot size of an incident light. The thicknesses of the Ge NM, SU-8, and PET were measured to be 0.4, 1, and 180 μm using a profilometer, respectively. Reflection and transmission spectra of the reference SU-8/PET structure were measured to be approximately 9.8% and 86% in average at the wavelength of 1000 ~ 1600 nm, respectively. (See Figure 4.7). In theory, the absorption (*A*) in the Ge layer can be calculated using the equation:

$A = 1\text{-}R\text{-}T$ (3)

where R and T refer to reflection and transmission, respectively.[32] The calculated absorption of 4.2% (Figure 4.7) of the SU8/PET stack was not the ideal value, because absorption in the SU-8/PET stack was negligible, considering that the extinction coefficients of the SU-8 and PET are nearly zero in the near IR wavelength range. The possible, but negligible, measurement error could be from the scattering loss at the surface caused by non-ideal surface normal incidence and the focused non-collimated incident beam.

Figure 4.6(b) shows the reflection and transmission spectra of the Ge NM/SU-8/PET stack. The reflection was measured to be approximately 60% in the near IR range, except for the sharp drop near 1250 nm. Such optical characteristics can be ascribed to the Fabry-Perot oscillation due to finite thickness of PET substrate.[33] To accurately extract the absorption of the Ge NM from the measured reflection and transmission of the Ge NM/SU-8/PET stack, the following equation can be derived by considering the measurement error.

$$A_{GeNM} = 1 - R_{GeNM/SU-8/PET} - T_{GENM/SU-8/PET} - T_{GeNM} \times E_{SU-8/PET} \quad (4)$$

where A is the absorption, R the reflection, T the transmission, and E the measurement error. The measurement error (i.e., $E_{SU\text{-}8/PET}$) used in Eq. (4) refers to the value measured from the SU-8/PET stack. In the case of the Ge NM/SU-8/PET stack, the light that reaches the interface of the Ge NM and SU-8/PET will be T_{GeNM}, which should be incorporated in Eq. (4). Figure 4.6(c) shows the absorption spectrum of the Ge NM obtained by Eq. (4) in the wavelength range of 1000 ~ 1600 nm. The absorption gradually decreased from 44% at 1000 nm to 9% at 1526 nm, except for an abrupt increase of approximately 36% near 1240 nm. The absorption decreased sharply to 0% at 1572 nm, which agreed well with the measured extinction coefficient of Ge NM. The absorption

coefficient of the annealed Ge NM was calculated to be 105 cm^{-1} at 1570 nm, and the penetration depth was calculated to be 95 μm. There is no absorption at wavelengths larger than 1570 nm, which can be explained by the thinness (i.e., 400 nm) and penetration depth of the Ge NM.

To further compare the experimentally obtained spectra with theory and simulation, we obtained each spectrum using the following equations. Because the Ge NM is optically thin and polished, multiple reflections should be considered. The reflection, absorption, and transmission of the Ge NM were calculated numerically using the following equations.[34]

$$r = [(n-1)^2 + k^2]/[(n+1)^2 + k^2] \quad (5) \qquad R = r + [(1-r)^2 re^{-2\alpha t}/(1-r^2 e^{-2\alpha t})] \quad (6)$$

$$A = [(1-r)(1-e^{-\alpha t})/(1-re^{-\alpha t})] \quad (7) \qquad T = 1-R-A \quad (8)$$

where r is reflectivity, n is the refractive index, k is the extinction coefficient, α is the absorption coefficient, and t is the thickness. All parameters used in the calculation were the measured values. Besides the numerical calculation, a simulation was carried out using a three dimensional finite-difference time-domain (FDTD) software (Lumerical FDTD) to simulate the *T*, *R*, and *A* spectra. A vertically stacked structure of Ge NM/SU-8/PET with thicknesses of 0.4, 1, and 180 μm was used. Optical constants of the SU-8 and PET were taken from literature,[35,36] while the optical constants of the Ge NM were based on the experimental data. The SU-8 and PET were assumed to be lossless in the simulation. As shown in Figure 4.6(b) and (c), very good agreement was obtained among the measured, calculated, and simulated plots. The Fabry-Perot oscillation was not observed from the calculated spectra, because the SU-8/PET substrate was not considered in the calculation.

Figure 4.6(d) shows comparative absorption spectra of the Ge (not H implanted), non-annealed, and annealed Ge NM in the same wavelength range. The absorption of Ge with the same

thickness of 400 nm was calculated using the optical constants measured by the ellipsometer. The inset of Figure 4.6(d) shows magnified spectra in the wavelength of 1500 ~ 1600 nm. It was observed that the absorptions of the non-annealed and annealed Ge NMs were slightly improved compared to that of the Ge across the measured wavelength. Zero absorption occurred at 1578 nm and beyond in the case of the Ge and the annealed Ge NM. However, the absorption of the non-annealed Ge NM extended to a longer wavelength, close to 1600 nm. In particular, the non-annealed Ge NM showed 0.8% of the absorption even at 1600 nm.

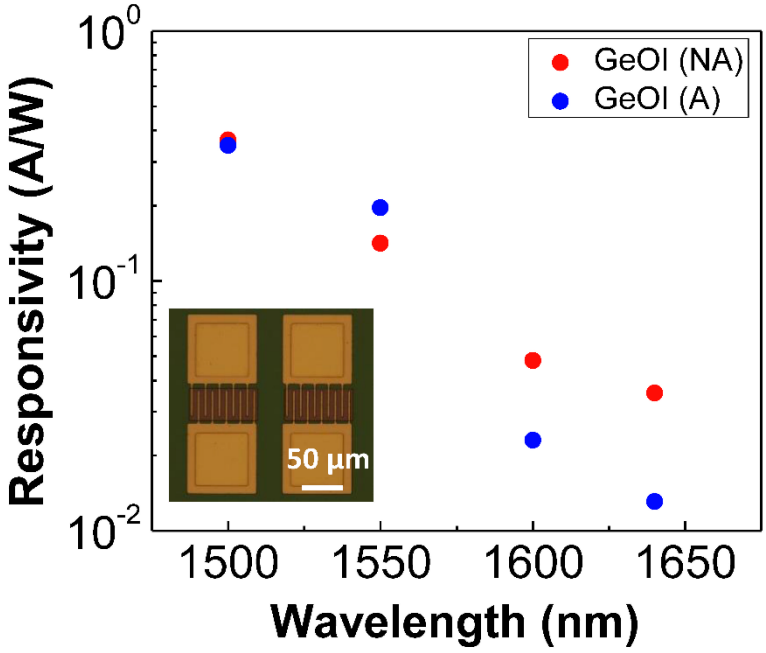

Figure 4.8. *Measured responsivity spectra of the MSM Ge photodiodes using the non-annealed (NA) and annealed (A) GeOI wafers at a wavelength range of 1.5 ~ 1.64 µm with a wavelength step of 50 nm. Inset shows a microscopic image of the fabricated MSM photodiodes.*

MSM Ge NM-based photodiodes were fabricated using non-annealed and annealed GeOI wafers. Figure 4.8 shows a comparison of typical responsivity spectra of the photodiodes at 2 V bias. Responsivity of the device with non-annealed Ge NM was constantly higher than that of the

device with annealed Ge NM under near IR illumination, except for that at 1550 nm. The responsivity at 1600 and 1640 nm increased from 0.023 A/W and 0.013 A/W to 0.048 A/W and 0.036 A/W, respectively. The enhanced responsivity of non-annealed cases at 1500, 1600, 1640 nm was consistent with the absorption spectra of the Ge NM as shown in Figure 4.6(d). It should be noted that the measured dark current of the device with the non-annealed Ge NM was 6.95 μA, which was higher than the annealed case (4.84 μA) at 2 V bias. This agreed well with the larger free-carrier concentration of the non-annealed Ge NM since the free carriers contribute to electrical conductivity. Overall, the improved photo-responsivity of the Ge photodiode demonstrated merits of engineering absorption in Ge NM using H ion implantation.

4.4 Conclusion

In summary, we have demonstrated the use of H ion implantation to enhance light absorption in Ge to extend its useful wavelength range for photon detection. The refractive index of the Ge layer of the GeOI wafer after H+ ion implantation decreased with a Δn of 0.024, while the extinction coefficient increased with a Δk of 0.027 compared to those of the bulk Ge wafer at the wavelength range of 1000 ~ 1600 nm, respectively. Although annealing further decreased the refractive index with an additional Δn of 0.022, it slightly decreased the extinction coefficient, having a Δk of 0.008 compared to that of the Ge layer of non-annealed GeOI wafer. Based on the measured optical constants, the absorption coefficient of the non-annealed GeOI wafer was calculated to be 224 cm^{-1} at 1600 nm, 10 times larger than that of the bulk Ge wafer (i.e., 22 cm^{-1}) and about 5 times larger than that of the annealed GeOI wafer (i.e., 40 cm^{-1}). The enhanced light absorption of H implanted Ge was further characterized on transferred Ge NMs on PET substrates. Absorption of the bulk Ge wafer and annealed Ge NM with the same thickness of 400 nm dropped

to zero at 1578 nm, whereas absorption wavelength of the non-annealed Ge NM was extended over 1600 nm. The measured responsivity spectra of Ge photodiodes exhibited the same behavior as the absorption spectra of the Ge NMs. Overall, H ion implantation provides an effective pathway towards enhancing light absorption in Ge, and can be applicable in high performance Ge based optoelectronic devices.

4.5 Reference

1 R. Soref, "Mid-infrared photonics in silicon and germanium", *Nature Photonics*, **4**, 495-496 (2010).

2 W. C. Dash and R. Newman, "Intrinsic optical absorption in single-crystal germanium and silicon at 77℃ and 300℃", *Phys. Rev.* 99, 1151 (1955).

3 E. Sackinger, *Broadband Circuits for Optical Fiber Communication* (John Wiley & Sons, Inc., 2005).

4 Y. Huang, J. Song, X. Luo, T.-Y Liow, and G.-Q. Lo, "CMOS compatible monilithic multi-layer Si_3N_4-on-SOI platform for low-loss high performance silicon photonics dense integration", Optics Express, Vol. 22, No. 18, pp. 21859-21865 (2014).

5 E. D. Palik, *Handbook of Optical Constants of Solids* (Academic Press NY, 1985).

6 S. Su, B. Cheng, C. Xue, W. Wang, Q. Cao, H. Xue, W. Hu, G. Zhang, Y. Zuo, and Q. Wang, "GeSn p-i-n photodetector for all telecommunication bands detection", *Optics Express*, Vol. 19, Issue 7, pp. 6400-6405 (2011).

7 J. Liu, D. D. Cannon, K. Wada, Y. Ishikawa, S. Jongthammanurak, D. T. Danielson, J. Michel, and L. C. Kimerling, "Tensile strained Ge photodetectors on Si platform for C and L band telecommunications", *Appl. Phys. Lett.* **87**, 011110 (2005).

8 J. R. Sanchez-Perez, C. Boztug, F. Chen, F. F. Sudradjat, D. M. Paskiewicz, R. B. Jacobson, M. G. Lagally, and R. Paiella, "Direct-bandgap light-emitting germanium in tensilely strained nanomembranes", *Proc. Natl. Acad. Sci. U. S. A.* 108(47), 18893–18898 (2011).

9 J. Liu, X. Sun, L. C. Kimerling, and J. Michel, "Direct-gap optical gain of Ge on Si at room temperature", *Optics Letters*, Vol. 34, Issue 11, pp. 1738-1740 (2009).

10 H.-C. Yuan, J. Shin, G. Qin, L. Sun, P. Bhattacharya, M. G. Lagally, G. K. Celler, and Z. Ma, "Flexible photodetectors on plastic substrates by use of printing transferred single-crystal germanium membranes", *Appl. Phys. Lett.* **94**, 013102 (2009).

11 J. R. Jain, A. Hryciw, T. M. Baer, D. A. B. Miller, M. L. Brongersma, and R. T. Howe, "A micromachining-based technology for enhancing germanium light emission via tensile strain", *Nature photon.*, **6**, 398-405 (2012).

12 W. S. Ho, Y.-H. Dai, Y. Deng, C.-H. Lin, Y.-Y. Chen, C.-H. Lee, and C. W. Liu, "Flexible Ge-on-polyimide detectors", *Appl. Phys. Lett.* **94**, 261107 (2009).

13 C. J. Tracy, P. Fejes, N. D. Theodore, P. Maniar, E. Johnson, A. J. Lamm, A. M. Paler, I. J. Malik, P. Ong, "Germanium-on-Insulator Substrates by Wafer Bonding", *Journal of Electronic Materials*, Vol. 33, Issue 8, pp. 886-892 (2004).

14 J. M. Zahler, A. F. i Morral, M. J. Griggs, H. A. Atwater, and Y. J. Chabal, "Role of hydrogen in hydrogen-induced layer exfoliation of germanium", *Physical Review B* **75**, 035309 (2007).

15 Y.-L. Chao, R. Scholz, M. Reiche, U. Gosele, and J. C. S. Woo, "Characteristics of Germanium-on-Insulators Fabricated by Wafer Bonding and Hydrogen-Induced Layer Splitting", *Japanese Journal of Applied Physics*, Vol. 45, No. 11, pp.8565-8570 (2006).

16 A. H. Kahn, "Theory of the Infrared Absorption of Carriers in Germanium and Silicon", *Physical Review*, Vol.97, No.6, pp.1647-1652 (1955).

17 V. Sorianello, L. Colace, N. Armani, F. Ross, C. Ferrari, L. Lazzarini, and G. Assanto, "Low-temperature germanium thin films on silicon," Opt. Mater. Express **1**(5), 856–865 (2011).

18 J. M. Zavada, H. A. Jenkinson, R. G. Sarkis, and R. G. Wilson, "Hydrogen depth profiles and optical characterization of annealed, proton-implanted n-type GaAs", *J. Appl. Phys.* **58**, 3731 (1985).

19 I. P. Ferain, K. Y. Byun, C. A. Colinge, S. Brightup, and M. S. Goorsky, "Low temperature exfoliation process in hydrogen-implanted germanium layers", *J. Appl. Phys.* **107**, 054315 (2010).

20 F. Fournel, H. Moriceau, and R. Beneyton, "Low temperature void free hydrophilic or hydrophobic silicon direct bonding", *ECS Trans.* **3**, 139 (2006).

21 K. Zhang, J.-H. Seo, W. Zhou, and Z. Ma, "Fast flexible electronics using transferrable silicon nanomembranes", *J. Phys. D: Appl. Phys.* **45**, 143001 (2012).

22 T. Akatsu, C. Deguet, L. Sanchez, F. Allibert, D. Rouchon, T. Signamarcheix, C. Richtarch, A. Boussagol, V. Loup, F. Mazen, J.-M. Hartmann, Y. Campidelli, L. Clavelier, F. Letertre, N. Kernevez, C. Mazure, "Germanium-on-insulator (GeOI) substrates-A novel engineered substrate for future high performance devices", *Materials Science in Semiconductor Processing*, Vol. 9. Issues 4-5, pp.444-448 (2006).

23 D. K. Schroder, *Semiconductor Material and Device Characterization* (WILEY, 1990).

24 P. D. Townsend, L. Zhang, P. J. Chandler, *Optical Effects of Ion Implantation* (CAMBRIDGE, 1994).

25 A. G. Foyt, W. T. Lindley, C. M. Wolfe, and J. P. Donnelly, "Isolation of junction devices in GaAs using proton bombardment", *Solid State Electron.* **12**, 209 (1969).

26 E. Garmire, H. Stoll, A. Yariv, and R. G. Hunsperger, "Optical waveguiding in proton-implanted GaAs", *Appl. Phys. Lett.* **21**, 87 (1972).

27 J. P. van der Ziel, W. T. Tsang, R. A. Logan, and W. M. Augustyniak, "Subpicosecond pulses from passively mode-locked GaAs buried optical guide semiconductor lasers", *Appl. Phys. Lett.* **39**, 376 (1981).

28 S. J. Pearton, J. W. Corbett, and T. S. Shi, "Hydrogen in Crystalline Semiconductors", *Appl. Phys. A*, 43, pp.153-195 (1987).

29 H. R. Philipp and E. A. Taft, "Optical Constants of Germanium in the Region 1 to 10 ev," Phys. Rev. **113**(4), 1002-1005 (1959).

30 R. A. Soref and B. R. Bennett, "Electrooptical Effects in Silicon," IEEE J. Quantum Electron. **QE-23**(1), 123-129 (1987).

31 J. Michel, J. Liu, and L. C. Kimerling, "High-performance Ge-on-Si photodetectors," Nat. Photonics **4**(7), 527-534 (2010).

32 E. D. Capron and O. L. Brill, "Absorption Coefficient as a Function of Resistance for Optical Germanium at 10.6 μm", *Applied Optics*, Vol. 12, Issue 3, pp.569-572 (1973).

33 S. Logothetidis, “Polymeric Substrates and Encapsulation for Flexible Electronics: Bonding Structure, Surface Modification and Functional Nanolayer Growth”, *Rev. Adv. Mater. Sci.* 10, pp.387-397 (2005).

34 P. W. Kruse, L. D. McGlauchlin, and R. B. McQuistan, *Elements of Infrared Technology* (WEILY, 1962).

35 J. L. Digaum, J. J. Pazos, J. Chiles, J. D’ Archangel, G. Padilla, A. Tatulian, R. C. Rumpf, S. Fathpour, G. D. Boreman, and S. M. Kuebler, “Tight control of light beams in photonic crystals with spatially-variant lattice orientation”, *Optics Express*, Vol. 22, Issue 21, pp.25788-25804 (2014).

36 J. F. Elman, J. Greener, C. M. Herzinger, and B. Johs, “Characterization of biaxially-stretched plastic films by generalized ellipsometry”, *Thin Solid Films*, Vol. 313-314, pp.814-818 (1998).

Chapter 5. Flexible Ge nanomembrane metal-semiconductor-metal (MSM) photodiodes

5.1 Introduction

Germanium (Ge) has been widely used in near infrared (NIR) photodetection on account of its large absorption coefficient at NIR wavelengths and compatibility with the modern Si CMOS technology.[1-5] Flexible Ge photodetector is of great interest in recent years as it provides favorable characteristics such as light-weight and bendability. A thin Ge layer has been formed on flexible substrates via various transfer techniques.[6,7] In particular, single crystalline Ge nanomembrane (Ge NM) released from Ge on insulator (GeOI) wafer can offer a thickness range from tens to hundreds of nanometers.[8] In addition, the doping type and concentration of Ge NM can be controlled via the choice of its donor wafer and ion implantation beforehand. Metal-semiconductor-metal (MSM) photodiodes show great advantages such as low capacitance and easy integration.[9] MSM structure can be easily formed without dopant diffusion such as ion implantation and spin on dopant (SOD).[10] However, large dark current is a critical drawback in Ge MSM photodiodes due to small bandgap energy. Low-doped Ge can be used in MSM photodiodes to overcome the large dark current because no ohmic contacts are required. Therefore, the combination of the low-doped Ge NM and MSM structure could be an ideal solution for low cost flexible Ge photodetectors. Although flexible Ge photodetectors with various device types (i.e., metal-insulator-semiconductor (MIS) and p-i-n (PIN)) have been reported, the bending effects on the photodetector characteristics have not been examined yet.[6,7] Here, we report the fabrication and characterization of flexible Ge NM MSM photodiodes. GeOI wafer, a source material, was fabricated by wafer bonding and Smart-Cut^{R} technology. The device was characterized on bending fixture to examine

strain-induced effects. The applied strain was quantified by Raman spectroscopy and NIR light with multiple wavelengths (i.e., 1.5, 1.55, 1.6, and 1.64 μm) was focused on the device to measure the photo response. We investigated the correlation between the amount of strain and dark current and photo responsivity of the photodiode.

5.2 Experiment

Four inch GeOI wafers were fabricated using a direct wafer bonding technique followed by Smart-Cut® process.[11] The fabrication began with unintentionally doped Ge wafer ($\rho > 40\ \Omega\cdot$cm) which corresponds to a doping concentration of less than 3.7×10^{13} cm^{-3}. Detailed procedure of GeOI wafer fabrication can be found elsewhere.[11] In short, hydrogen (H) ions (dose: 1×10^{17} cm^{-2} and energy: 100 keV) were ion implanted on a Ge wafer capped with a 100 nm thick plasma enhanced chemical vapor deposition (PECVD) SiO_2, followed by the direct bonding with a Si wafer coated with a 300 nm thick thermal oxide. An 800 nm thick Ge layer was exfoliated from the Ge wafer and successfully transferred onto the oxidized Si wafer using a two-step annealing process (200℃ for 3 hours and 250℃ for 1 hour). The rough Ge surface which was damaged during the implantation process was then chemically and mechanically polished and achieved a 400 nm Ge layer thickness with a 0.656 nm root mean square (RMS) surface roughness. Figure 5.1(a) shows an optical image of the finished GeOI wafer.

Figure 5.1(b) shows a schematic process flow of flexible Ge NM MSM photodiodes. The process began with the GeOI wafer (Figure 5.1(b) i)) followed by the release and transfer of the Ge layer. A top Ge layer was patterned to an array of Ge islands (size: $40 \times 80\ \mu m^2$) using reactive ion etching (RIE). A SiO_2 buried oxide layer was selectively etched by hydrofluoric acid (HF, 49%) and the Ge layer, now called Ge NM, was released and (Figure 5.1(b) ii)) flip-transferred

onto the adhesive layer (SU8-2002) coated polyethylene terephthalate (PET) substrate (Figure 5.1(b) iii)). Interdigitated metal electrodes (Ti/Au = 50/450 nm) with a 2 μm width and a 6 μm distance between the electrodes were e-beam evaporated on the transferred Ge NMs and lifted off (Figure 5.1(b) iv)). Figure 5.1(c) and (d) show an optical image of flexible Ge NM MSM photodiodes on a bent PET substrate and a microscopic image of the array of the photodiodes, respectively.

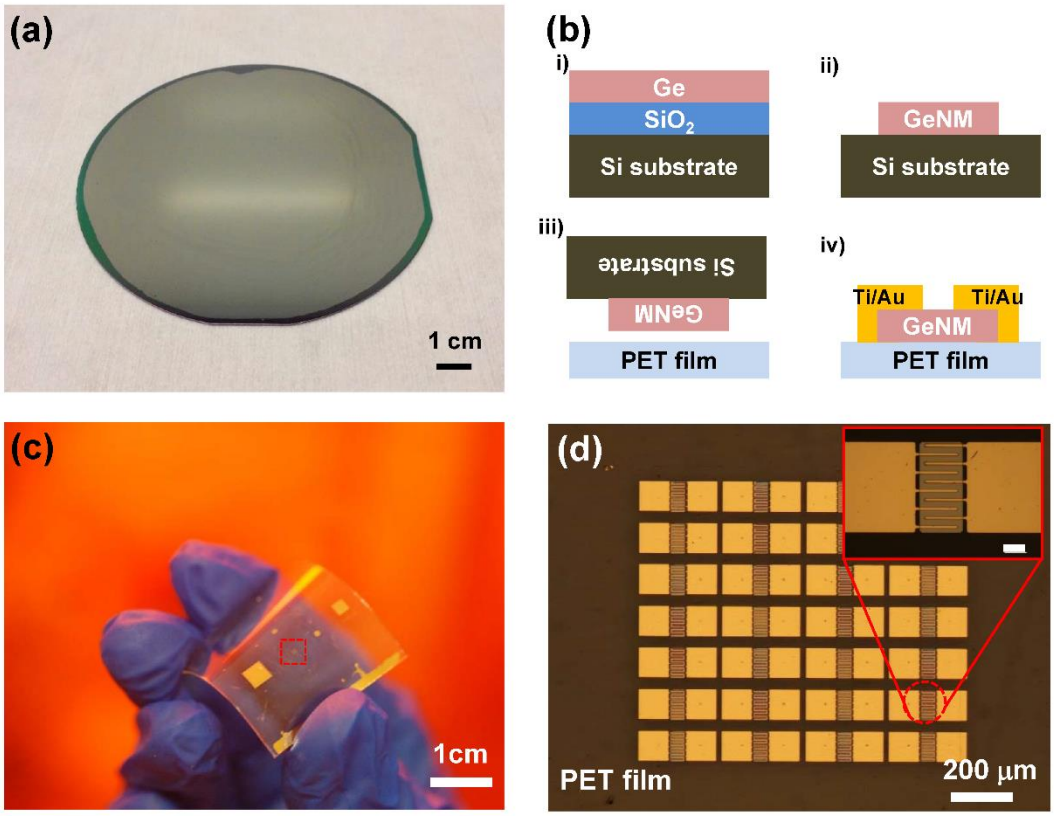

Figure 5.1. (a) *An optical image of the fabricated 4-inch GeOI wafer.* ***(b)*** *A schematic process flow for Ge nanomembrane (Ge NM)-based metal-semiconductor- metal (MSM) photodiode on flexible substrate: i) Process begins with the fabrication of Ge on insulator (GeOI) wafer with a 400 nm thick top Ge template layer and a 300 nm thick buried oxide layer. ii) Ge NM released from the GeOI wafer using 49% hydrofluoric (HF) acid. iii) Ge NM transferred on polyethylene*

terephthalate (PET) film coated with an adhesive layer (SU8-2002). iv) Metal electrodes (Ti/Au= 50/450 nm) deposited by e-beam evaporation and lift-off. ***(c)*** *An optical image of the array of Ge NM MSM photodiodes on a bent PET substrate.* ***(d)*** *A microscopic image of the flexible Ge NM MSM photodiodes on PET substrate. Inset shows the image of an individual device. Scale bar in inset is 20 μm.*

5.3 Experimental Results and Discussion

The sample was mounted on convex fixtures with radius ranging from 77.5 to 21 mm. The strain created by fixtures was calculated by Horiba LabRAM ARAMIS Raman spectroscopy. A 532 nm green laser was used to focus the surface of the Ge NM with a 100× objective lens. Figure 5.2(a) shows the correlation between radii of the fixtures and induced tensile strain. Inset of Figure 5.2(a) shows Raman spectra measured from the Ge NMs under the flat condition and bent PET substrate (Radius= 21 mm), respectively. The Raman scattering peak by the Ge-Ge vibration modes for the Ge NM appeared at 320.29 cm^{-1} without strain. The Ge Raman peaks measured under bending conditions were shifted to a smaller wavenumber, indicating that tensile strain was induced by the bending fixtures.

The uniaxial tensile strain in (001) Ge can be extracted based on the Raman shift using the following equation:[12]

$$\varepsilon(\%) = -0.495 \times \Delta\omega(cm^{-1}) \qquad (1)$$

where ε is the uniaxial strain along the <110> direction and $\Delta\omega$ is the Raman peak shift. The Raman peak shifts of the Ge NMs bent along the <110> direction on the fixtures with radii of 77.5, 38.5, and 21 mm were measured to be 0.22, 0.46, and 0.84 cm^{-1}, respectively. Using Eq. (1), the uniaxial

tensile strain of bent Ge NMs were calculated to be 0.11, 0.23, and 0.42%, respectively. Strain values extracted from Raman spectroscopy was confirmed with strain values associated with bending fixtures using the following equation:[13]

$$\varepsilon(\%) = \frac{1}{2R(mm)/T(\mu m)+1} \qquad (2)$$

where R is the radius of the fixture and T is the thickness of the bent object (μm). T includes the thicknesses of the PET film (175 μm), the adhesive layer (1 μm), and the Ge NM (0.4 μm). The uniaxial tensile strains corresponding to radii of 77.5, 38.5, and 21 mm were calculated to be 0.11, 0.23, and 0.42%, which agreed well with values from Raman results.

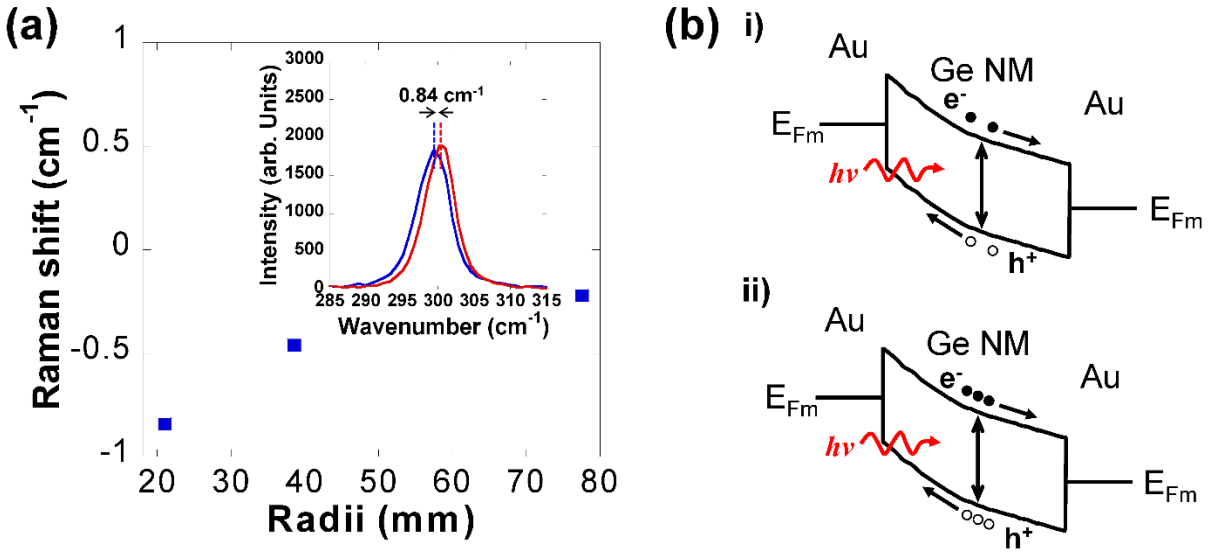

Figure 5.2. (a) *Raman shift corresponding to the radius of bending fixture. Inset shows Raman peak shift of 0.84 cm^{-1} measured from the Ge NMs under flat condition (Red) and the fixture with radius of 21 mm (Blue).* ***(b)*** *The band diagram of the Ge NM based MSM photodiode: i) without strain. ii) under the tensile strain.*

Figure 5.2(b) shows the band diagram of the MSM photodiode under applied forward bias which exceeds the flat-band voltage. When photons with larger energy than the bandgap of Ge

(i.e., 0.66 eV) is absorbed, electron-hole pairs are generated and swept separately by the built-in electric field (See Figure 5.2(b) i)). Since the absorption coefficient of Ge is greater under tensile strain,[14] more electron-hole pairs are generated by the same condition, leading to increased photo currents (See Figure 5.2(b) ii)). Also, a reduced Schottky barrier height between the strained Ge NM and a metal contact is attributed to the split valence band, compared to the unstrained Ge. However, the photo current increased by this effect is negligible because the barrier height is significantly lowered at the forward bias.

Current-voltage characteristics of Ge NM based MSM photodiodes were measured by a HP4155B semiconductor parameter analyzer under dark and illuminated conditions. An infrared light source with various wavelengths (i.e., 1.5, 1.55, 1.6, and 1.64 μm) from a tunable external cavity laser (TUNICS-*Plus*) was used to focus the devices via a lensed fiber. The output powers from the lensed fiber at different wavelengths were measured by a laser power meter (Edmund Coherent® FieldMate). The Ge NM photodiodes were initially characterized under the flat condition (i.e., without strain). Figure 5.3(a) shows dark and photocurrent of the Ge NM photodiode at a bias range from 0 to 3 V. Figure 5.3(b) shows the responsivity as a function of wavelength at 2 and 3 V voltage bias conditions. The responsivity values were measured to be 0.17 and 0.20 A/W under a wavelength of 1.5 μm at 2 and 3 V, respectively, which continuously decreased with increasing wavelength. This trend is ascribed to the sharp reduction of the absorption coefficient of Ge at 1.5 μm. Namely, the absorption coefficient of Ge is 5×10^3 cm^{-1} at 1.5 μm, and decreases to 60 cm^{-1} at 1.6 μm.[15] Figure 5.3(d) shows the responsivity as a function of optical power at 1.55 μm and V = 2 and 3 V. As expected, the responsivity slightly decreased from 0.027 to 0.019 A/W at 3 V as the optical power is increased from 55 to 220 μW. However, the photocurrent gradually increased under the same optical power range and the same wavelength

as shown in Figure 5.3(c). The result indicates that photo-generated carriers are responsible for the generated photocurrent under illumination.

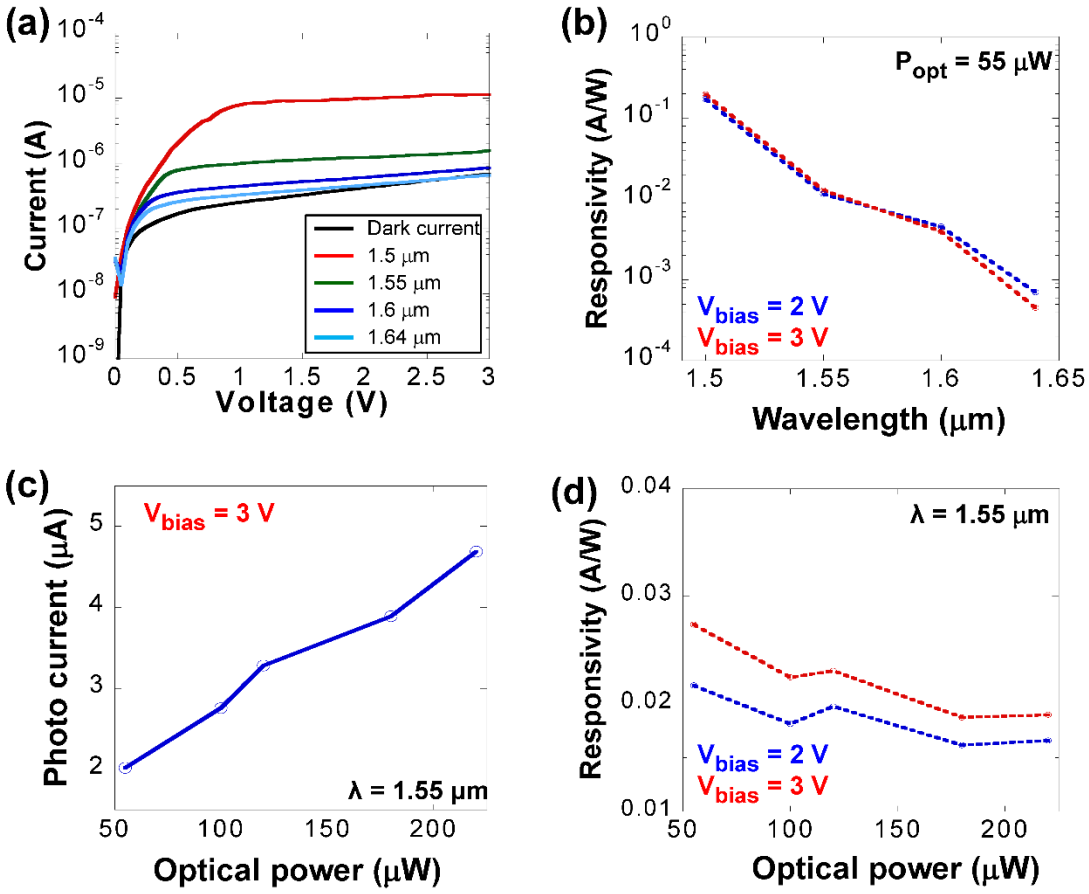

Figure 5.3. ***(a)*** *The measured dark and photo current at various wavelengths 1.5, 1.55, 1.6, and 1.64 μm.* ***(b)*** *Typical responsivity spectra of photodiode as a function of wavelength without strain at 2 and 3 V.* ***(c)*** *The measured photo currents (wavelength: 1.55 μm) at 3 V with different optical powers of 55, 100, 120, 180, and 220 μW.* ***(d)*** *Typical responsivity spectrum of photodiode as a function of optical power at 1.55 μm without strain at 2 and 3 V.*

To further investigate the correlation between the optical property and the strain, the performance changes of Ge NM photodiodes by the uniaxial tensile strain were evaluated. Figure 5.4(a) shows the measured dark current density under various degrees of strain. The dark current

density was measured to be 21.5 mA/cm^2 at 3 V without strain. It should be noted that the dark current density is lower than those of reported Ge MSM photodiodes which typically are on the order of 100 mA/cm^2.[16,17] This low dark current density demonstrates the high quality of the transferred Ge NM. The dark current density constantly decreased to 14.8, 8.5, and 4.8 mA/cm^2 under the strain of 0.11, 0.23, and 0.42%, respectively. The suppression of the dark current was attributed to the splitting of the valence bands of Ge NM into light-hole (LH)/heavy-hole (HH) under the uniaxial tensile strain.[18] Because the top of the valence band of Ge NM is composed of the LH band, intrinsic carrier density is decreased by the reduction of the density of states for holes, leading to the suppressed dark current.[19]

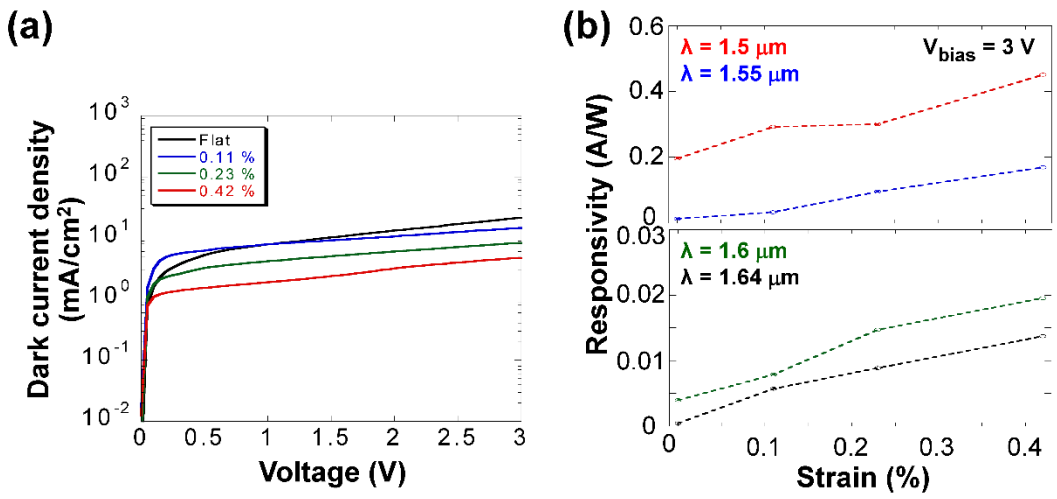

Figure 5.4. (a) *Dark current density versus voltage bias measured under uniaxial tensile strain.* ***(b)*** *Typical responsivity spectra as a function of the different strain at various wavelengths.*

Figure 5.4(b) shows the responsivity as a function of strain at wavelengths 1.5, 1.55, 1.6, and 1.64 μm. The responsivity was measured to be 0.2 A/W without strain, while it increased to 0.29, 0.3, and 0.45 A/W under 0.11, 0.23, and 0.42% strain, respectively, at 1.5 μm. In addition, the responsivity values were also enhanced at longer wavelengths as the strain is increased. Since

the indirect bandgap energy at the L valley decreases faster than the direct bandgap energy at the Γ valley under the tensile strain, a relative enhancement in the optical property of Ge NM is expected. In order to examine the strain effect in Ge, the bandgap shrinkage was calculated using deformation potentials of Ge.[20] Theoretical calculation reveals that the energy difference between the Γ and L valleys is reduced from 133 meV (i.e., unstrained Ge) to 122 meV under 0.42% uniaxial tensile strain. The result suggests that an absorption edge of Ge expands toward lower energy (i.e., longer wavelength), allowing the detection range of the photodetector to cover a wavelength longer than 1.5 μm. Overall, tensile strained Ge NM based MSM photodiodes exhibit the enhancements in performance of not only low dark current, but also high responsivity.

5.4 Conclusion

In summary, we have demonstrated flexible Ge NM based MSM photodiodes on PET substrate. The optical and electrical characteristics of the uniaxial tensile strained photodiodes were investigated. The dark current density of the photodiode was reduced from 17.2 to 3.8 mA/cm^2 at 3 V and the responsivity was increased from 0.2 to 0.45 A/W at 1.5 μm by 0.42% strain. In addition, the enhancement in the responsivity was also observed at longer wavelengths up to 1.64 μm. Improved performance such as dark current reduction and responsivity increase is ascribed to the bandgap shrinkage induced by tensile strain.

5.5 Reference

1 J. Michel, J. Liu, and L. C. Kimerling, "High-performance Ge-on-Si photodetectors", *Nature Photonics* 4, 527-534 (2010).

2 Y. Kang, H.-D. Liu, M. Morse, M. J. Paniccia, M. Zadka, S. Litski, G. Sarid, A. Pauchard, Y.-H. Kuo, H.-W. Chen, W. S. Zaoui, J. E. Bowers, A. Beling, D. C. McIntosh, X. Zheng, and J. C. Campbell, "Monolithic germanium/silicon avalanche photodiodes with 340 GHz gain–bandwidth product", *Nature Photonics* 3, 59-63 (2009).

3 D. Feng, S. Liao, P. Dong, N.-N Feng, H. Liang, D. Zheng, C.-C. Kung, J. Fong, R. Shafiiha, J. Cunningham, A. V. Krishnamoorthy, and M. Asghari, "High-speed Ge photodetector monolithically integrated with large cross-section silicon-on-insulator waveguide", *Appl. Phys. Lett.* 95, 261105 (2009).

4 L. Cao, J.-S. Park, P. Fan, B. Clemens, and M. L. Brongersma, "Resonant Germanium Nanoantenna Photodetectors", *Nano Lett.*, 10(4), pp. 1229-1233 (2010).

5 L. Vivien, J. Osmond, J.-M. Fedeli, D. Marris-Morini, P. Crozat, J.-F. Damlencourt, E. Cassan, Y. Lecunff, and S. Laval, "42 GHz p.i.n Germanium photodetector integrated in a silicon-on-insulator waveguide", *Optics Express* Vol. 17, Issue 8, pp. 6252-6257 (2009).

6 W. S. Ho, Y.-H. Dai, Y. Deng, C.-H. Lin, Y.-Y. Chen, C.-H. Lee, and C. W. Liu, "Flexible Ge-on-polyimide detectors", *Appl. Phys. Lett.* 94, 261107 (2009).

7 H.-Y. Yuan, J. Shin, G. Qin, L. Sun, P. Bhattacharya, M. G. Lagally, G. K. Celler, and Z. Ma, "Flexible photodetectors on plastic substrates by use of printing transferred single-crystal germanium membranes", *Appl. Phys. Lett.* 94, 013102 (2009).

8 J. R. Sanchez-Perez, C. Boztug, F. Chen, F. F. Sudradjat, D. M. Paskiewicz, R. B. Jacobson, M. G. Lagally, and R. Paiella, "Direct-bandgap light-emitting germanium in tensilely strained nanomembranes", *Proc. Natl. Acad. Sci. U. S. A.* 108(47), 18893-18898 (2011).

9 B. L. Sharma, *Metal-Semiconductor Schottky Barrier Junctions and Their Applications* (Plenum Press NY, 1984).

10 L. Colace, G. Masini, F. Galluzzi, G. Assanto, G. Capellini, L. D. Gaspare, E. Palange, and F. Evangelisti, "Metal–semiconductor–metal near-infrared light detector based on epitaxial Ge/Si", *Appl. Phys. Lett.* 72, 3175 (1998).

11 T. Akatsu, C. Deguet, L. Sanchez, F. Allibert, D. Rouchon, T. Signamarcheix, C. Richtarch, A. Boussagol, V. Loup, F. Mazen, J.-M. Hartmann, Y. Campidelli, L. Clavelier, F. Letertre, N. Kernevez, and C. Mazure, "Germanium-on-insulator (GeOI) substrates—A novel engineered substrate for future high performance devices", *Materials Science in Semiconductor Processing* 9, pp. 444-448 (2006).

12 C.-Y. Peng, C. –F. Huang, Y.-C. Fu, Y.-H. Yang, C.-Y. Lai, S.-T. Chang, and C. W. Liu, "Comprehensive study of the Raman shifts of strained silicon and germanium", *J. Appl. Phys.* 105, 083537 (2009).

13 G. Qin, L. Yang, J.-H. Seo, H.-C. Yuan, G. K. Celler, J. Ma, and Z. Ma, "Experimental characterization and modeling of the bending strain effect on flexible microwave diodes and switches on plastic substrate", *Appl. Phys. Lett.* 99, 243104 (2011).

14 D. D. Cannon, J. Liu, Y. Ishikawa, K. Wada, D. T. Danielson, S. Jongthammanurak, J. Michel, and L. C. Kimerling, "Tensile strained epitaxial Ge films on Si(100) substrates with potential application in *L*-band telecommunications", *Appl. Phys. Lett.* 84, 906 (2004).

15 E. D. Palik, *Handbook of Optical Constants of Solids* (Academic Press NY, 1985).

16 H. Zang, S. J. Lee, W. Y. Loh, J. Wang, M. B. Yu, G. Q. Lo, D. L. Kwong, and B. J. Cho, "Application of dopant segregation to metal-germanium-metal photodetectors and its dark current suppression mechanism", *Appl. Phys. Lett.* 92, 051110 (2008).

17 K.-W. Ang, S.-Y. Zhu, J. Wang, K.-T. Chua, M.-B. Yu, G.-Q. Lo, and D.-L. Kwong, "Novel Silicon-Carbon (Si:C) Schottky Barrier Enhancement Layer for Dark-Current Suppression in Ge-on-SOI MSM Photodetectors", *IEEE Electron Device Lett.* Vol. 29, No. 7 (2008).

18 J. R. Jain, A. Hryciw, T. M. Baer, D. A. B. Miller, M. L. Brongersma, and R. T. Howe, "A micromachining-based technology for enhancing germanium light emission via tensile strain", *Nature Photonics* 6, 398-405 (2012).

19 Y. Ishikawa, K. Wada, D. D. Cannon, J. Liu, H.-C. Luan, and L. C. Kimerling, "Strain-induced band gap shrinkage in Ge grown on Si substrate", *Appl. Phys. Lett.* 82, 2044 (2003).

20 Van der Walle, C. G. "Band lineups and deformation potentials in the model-solid theory", *Phys. Rev. B* Vol. 39, No. 3, pp.1871-1883 (1989).

Chapter 6. Future work

Si NM based DB and TB RTDs were demonstrated in Chapter 3 and NDR with a high PVCR was measured at room temperature. Removing Si NMs with thicknesses of less than 20 nm from the substrate produces cracks which reduce the size of the continuous film. To avoid this issue, RIE was processed on the transferred Si NM to further thin down the Si NM. However, it was well-known that the RIE could induce non-uniformity in thickness of the etched film. Non-uniform thickness of the Si NM (i.e., well layer) could be attributed to the performance variation of devices. Forming ultrathin Si NMs with minimum thickness variation can be a prospective goal. This can open new opportunities realizing circuit level applications such as oscillators or multiplexers.

Fabrication and characterization of GeOI wafer were demonstrated in Chapter 4. Although we showed i-type (unintentionally doped) GeOI wafers in the thesis, p-type (Ga-doped) and n-type (Sb-doped) GeOI wafers with doping concentrations of $1\times10^{17} \sim 1\times10^{18}$ cm^{-3} were also fabricated. However, some applications require GeOI wafers with a very high doping concentration exceeding 1×10^{19} cm^{-3}. Fabricating GeOI wafers with doping concentration larger than 1×10^{19} cm^{-3} can be our next goal, which will increase versatility of the GeOI wafers.